

to be submitted to ApJ

# High Resolution Observations and Modeling of Dynamic Fibrils

B. De Pontieu

*Lockheed Martin Solar and Astrophysics Lab, 3251 Hanover St., Org. ADBS, Bldg. 252,  
Palo Alto, CA 94304, USA*

`bdp@lmsal.com`

V.H. Hansteen<sup>1</sup>

*Institute of Theoretical Astrophysics, University of Oslo, PO Box 1029 Blindern, 0315  
Oslo, Norway*

`viggo.hansteen@astro.uio.no`

L. Rouppe van der Voort<sup>1</sup>

*Institute of Theoretical Astrophysics, University of Oslo, PO Box 1029 Blindern, 0315  
Oslo, Norway*

`rouppe@astro.uio.no`

M. van Noort<sup>2</sup>

*Institute of Theoretical Astrophysics, University of Oslo, PO Box 1029 Blindern, 0315  
Oslo, Norway*

`noort@astro.su.se`

M. Carlsson<sup>1</sup>

*Institute of Theoretical Astrophysics, University of Oslo, PO Box 1029 Blindern, 0315  
Oslo, Norway*

`mats.carlsson@astro.uio.no`

---

<sup>2</sup>Now at: Institute for Solar Physics of the Royal Swedish Academy of Sciences, AlbaNova University Center, 106 91 Stockholm, Sweden

<sup>1</sup>Also at: Center of Mathematics for Applications, University of Oslo, P.O. Box 1053, Blindern, N-0316 Oslo, Norway

## ABSTRACT

We present unprecedented high resolution  $H\alpha$  observations, obtained with the Swedish 1-m Solar Telescope, that, for the first time, spatially and temporally resolve dynamic fibrils in active regions on the Sun. These jet-like features are similar to mottles or spicules in quiet Sun. We find that most of these fibrils follow almost perfect parabolic paths in their ascent and descent. We measure the properties of the parabolic paths taken by 257 fibrils, and present an overview of the deceleration, maximum velocity, maximum length and duration, as well as their widths and the thickness of a bright ring that often occurs above dynamic fibrils. We find that the observed deceleration of the projected path is typically only a fraction of solar gravity, and incompatible with a ballistic path at solar gravity. We report on significant differences of fibril properties between those occurring above a dense plage region, and those above a less dense plage region where the magnetic field seems more inclined from the vertical. We compare these findings to advanced numerical 2D radiative MHD simulations, and find that fibrils are most likely formed by chromospheric shock waves that occur when convective flows and global oscillations leak into the chromosphere along the field lines of magnetic flux concentrations. Detailed comparison of observed and simulated fibril properties shows striking similarities of the values for deceleration, maximum velocity, maximum length and duration. We compare our results with observations of mottles and find that a similar mechanism is most likely at work in the quiet Sun.

*Subject headings:* magnetic fields — Sun: photosphere — Sun: chromosphere

## 1. Introduction

The chromosphere is in a highly dynamic state, varying on timescales of minutes or less. Much of the dynamics in the magnetized regions associated with the magnetic network and plage are dominated by short-lived, jet-like features. A whole range of names has been applied to describe these chromospheric features. At the quiet Sun limb, they are traditionally called spicules, where they are observed in  $H\alpha$  as thin, elongated features that develop speeds of  $10\text{--}30\text{ km s}^{-1}$  and reach heights of on average  $5\text{--}9\text{ Mm}$  during their lifetimes of 3 to 15 minutes (Beckers 1968). Their widths ( $0.2\text{--}1\text{ Mm}$ ) and dynamics have, until recently, been very close to the resolution limits of observations. As a result of this limitation, the superposition inherent in limb observations, and the difficulty associated with interpreting  $H\alpha$  data, the

properties of spicules have not been very well constrained, which has led to a multitude of theoretical models (for a review, see, Sterling 2000). The same issues have plagued a solid identification of a counterpart to spicules on the disk. Observations on the disk in  $H\alpha$  reveal dark mottles in quiet Sun regions. These dark mottles seem similar to spicules, and usually appear in close association with small flux concentrations (and bright points) in the magnetic network that outlines the supergranular cells. There has been a long-standing discussion on whether spicules and mottles are the same phenomena. This discussion has focused on the different velocity distributions of mottles and spicules to conclude that mottles are not the disk counterpart of spicules (Grossmann-Doerth & Schmidt 1992). However, several groups have used more recent data to argue for a close relationship between mottles and spicules (see, e.g., Tsiropoula et al. 1994; Suematsu et al. 1995; Christopoulou et al. 2001).

Dynamic, jet-like features can also be seen in and around active region plage regions. These features are shorter (1-4 Mm) and shorter-lived (3-6 minutes) and appear to form a subset of what have traditionally been called active region fibrils. There are also fibrils that do not show jet-like behavior (Fig. 2). These are apparently low-lying, heavily inclined and more static loop-like structures that connect plage regions with opposite polarity magnetic flux. In the remainder of this paper, we will not discuss these low-lying fibrils, but focus on the motions of the shorter dynamic fibrils (hereafter abbreviated as DFs).

Only recently have DFs become the focus of detailed study, with several papers studying their dynamics, influence on the transition region and their oscillatory properties (De Pontieu et al. 1999, 2003b,a, 2004, 2005; Tziotziou et al. 2004). In the past, several authors have reported periodicities and oscillations in spicule observations, usually with dominant periods of order 5 minutes. Such periodicities in radial velocity, half-width and line intensity have been suggested based on older observations at the limb, but their interpretation has been difficult due to the complicated line formation of  $H\alpha$ , line-of-sight superposition and limited spatial resolution (Beckers 1968; Platov & Shilova 1971; Kulidzanishvili & Nikolskii 1978). More recently, De Pontieu et al. (2003a) have discovered significant oscillatory power in DFs in active regions using high-resolution data from the Swedish 1 m Solar Telescope (Scharmer et al. 2003a). Not all DFs show oscillations or recurrence, but a significant number do. Most of the power in especially more inclined DFs resides in periods between 4 and 6 minutes (De Pontieu et al. 2004; De Pontieu & Erdélyi 2006). Similar periods have been found by Tziotziou et al. (2004) in mottles in enhanced network or weak plage. De Pontieu et al. (2004) and De Pontieu & Erdélyi (2006) developed a new numerical model to explain the cause of these (quasi)periodic mottles or DFs. They compared their model to data from the Transition Region and Coronal Explorer (TRACE Handy et al. 1999) and suggested that inclined magnetic fields allow leakage of normally evanescent photospheric p-modes (which have dominant periods of 5 minutes) into the atmosphere where they form shocks that drive

DFs. A recent paper by Hansteen et al. (2006) uses extremely high resolution observations obtained at the SST and significantly more advanced numerical modelling to show that dynamic fibrils are indeed caused by magneto-acoustic shock waves.

In this paper, we directly expand on the work by Hansteen et al. (2006). Here we perform a more comprehensive analysis of the properties and motion of DFs using the same extremely high spatial and temporal resolution SST dataset of Hansteen et al. (2006). In addition, we use advanced 2/3D numerical radiative MHD simulations that include the convection zone, photosphere, chromosphere and lower corona to interpret all of the measurements and correlations found in the SST data analysis, many of which have not been described in Hansteen et al. (2006). In § 2 we discuss the details of the observations and instrumentation, including a description of a novel, advanced optical setup that allowed a diffraction limited 88 minute long timeseries in  $H\alpha$  linecenter. We describe the typical temporal evolution and measure properties of DFs in § 3. This section also deals with intriguing regional differences and correlations in DF properties that seem to be related to the oscillatory behavior of DFs. To interpret these findings, we use a numerical model that is described in § 4. This section also summarizes our observational findings and contains a more detailed description of the new model (introduced by Hansteen et al. 2006) that explains our observations. Our results strongly suggest that DFs naturally form as the result of chromospheric shock waves driven by convective flows and (global) oscillations in the photosphere as suggested by De Pontieu et al. (2004).

In § 4.4 we discuss in more detail how this model and our observations of active region DFs relate to equivalent quiet Sun phenomena. The dynamics of quiet Sun mottles have been studied extensively by several groups recently (Tsiropoula et al. 1994; Suematsu et al. 1995; Christopoulou et al. 2001; Tziotziou et al. 2003; Al et al. 2004; Tsiropoula & Tziotziou 2004; Tziotziou et al. 2004). While the lack of high spatial and temporal resolution data has made it difficult to properly interpret the findings, this recent work seems to have resolved a long-standing issue (Nishikawa 1988) regarding the paths mottles follow during their ascent and descent. Suematsu et al. (1995) and Christopoulou et al. (2001) use  $H\alpha$  data to establish that mottles follow parabolic paths. In fact, observations by Christopoulou et al. (2001) indicate that spicules at the limb similarly trace parabolic paths. Mottles initially appear in the blue wing of  $H\alpha$  extending in the process to lengths of some 2 to 8 Mm (Suematsu et al. 1995). After reaching maximum extent, they fade from the blue wing and appear in the red wing of  $H\alpha$  to recede generally along the same path. Throughout most of their lifetime they appear as dark, elongated features in  $H\alpha$  linecenter. The measurements of the parabolic paths traced by mottles have been difficult to interpret. The projected decelerations of the top of the mottle are generally observed to be far less than solar gravity. Attempts have been made to interpret such low decelerations as projection effects superposed on ballistic

flights. However, the projection angles necessary are typically not compatible with measured Doppler shifts (Suematsu et al. 1995), ruling out a purely ballistic interpretation. In addition, a purely ballistic flight would imply large initial velocities that have not been observed (Christopoulou et al. 2001; Suematsu et al. 1995). These observational findings have been difficult to reconcile with the plethora of models for spicules or mottles (Sterling 2000). In § 4.4 we describe the similarities between mottles and DFs in more detail, and discuss the applicability of our model to quiet Sun mottles. Our results are summarized in § 5.

## 2. Observations and Instrumentation

The observations were obtained with the Swedish 1-m Solar Telescope on La Palma. The Solar Optical Universal Polarimeter (SOUP, Title & Rosenberg 1981) was used to obtain narrow-band images in the linecenter of  $H\alpha$  (filter FWHM 12.8 pm). To compensate for seeing deformations in real-time, the observations were aided by the use of the SST adaptive optics system (AO, Scharmer et al. 2003b) consisting of a tip-tilt mirror, a bimorph mirror with 37 actuators, a correlation tracker, and a Shack–Hartmann wavefront sensor. As a further measure to reduce seeing aberrations, the data were post-processed with the Multi-Object Multi-Frame Blind Deconvolution image restoration method (MOMFBD, van Noort et al. 2005). This method is complementary to the use of AO since it reduces residual aberrations not corrected by the AO and it corrects the areas in the FOV that are not used for the AO wavefront sensing.

The science cameras consisted of 3 new, high speed cameras of type Sarnoff CAM1M100, with a CCD readout time of only 10 ms and an effective exposure time of 15 ms, resulting in a frame rate of approximately 37 frames-per-second (fps). The setup used was specially built for MOMFBD processing of the data and consisted of one camera behind the SOUP filter and 2 "wideband" cameras in front of the SOUP filter but after the SOUP pre-filter (a 0.8 nm FWHM interference filter centered at 656.3 nm). The light for the wideband cameras was split off the main beam by a 90/10 beamsplitter in front of the SOUP filter and split again evenly for the 2 wideband cameras, which were set up as a phase diversity pair with one camera at 12 mm defocus on a 45 m focal length. A schematic drawing of the red beam optical set-up is shown in Fig. 1.

To ensure simultaneous exposure, a specially designed chopper with a useful aperture of  $22 \times 22$  mm and a variable duty cycle of  $\frac{1}{2} - \frac{3}{4}$  was used as a shutter. To guarantee correct labeling of all camera frames, a unique exposure number was generated by the shutter electronics and stored on the camera PCs. This scheme guarantees that simultaneously exposed frames can be uniquely identified, a feature that is required for MOMFBD processing

but difficult to achieve using the internal clock of the observing PCs at the frame rates used.

The large data rate produced by the cameras ( $72 \text{ MB s}^{-1}$  per camera) was reduced by a factor of 3 using real-time data compression, sent from the camera computers to disk-writing computers through ordinary gigabit network connections, and then passed through fiberchannel links to the RAID controllers of an ATABeast system. More details of the data acquisition, as well as first results from this unique dataset are described by van Noort & Rouppe van der Voort (2006).

The observations were obtained on 04-Oct-2005 and consist of a time series of about 78 minute duration, centered on one of the larger spots in the young active region AR10813 at S7,E37. The observing angle  $\theta$  between the line-of-sight and the local vertical is  $39^\circ$  ( $\mu = \cos(\theta) = 0.78$ ). The field-of-view (FOV) was about  $64'' \times 64''$  at a pixel scale of  $0''.063$ . This corresponds to a FOV of  $46,400 \times 46,400 \text{ km}$ , with a pixel scale of  $45.7 \text{ km}$ . The diffraction limit of the SST at  $6563 \text{ \AA}$  is  $0.165''$ , i.e.,  $120 \text{ km}$ .

## 2.1. Data reduction

The images from all cameras were jointly processed with the MOMFBD image restoration method, yielding 2 restored images for each restoration (1 wide band and 1  $\text{H}\alpha$ ). Since the common field-of-view of the cameras within an MOMFBD set is separately aligned to sub-pixel accuracy, the restored images have near-perfect alignment.

Sets from 12 exposures were used per restoration (i.e., 36 images in total) resulting in a time series with 3 fps. For this study, we selected every third image, giving a time series with a fixed cadence of 1 s between images.

The time series were corrected for diurnal field rotation, aligned and de-stretched. The (local) offsets were determined on the wide band images and subsequently applied to the  $\text{H}\alpha$  images.

## 2.2. Description of field of view

The field of view of the time series contains two small sunspots of NOAA active region (AR) 10813. The larger of the spots is split into two parts by a lightbridge as seen in the left panel of Fig. 2. The spots are surrounded by areas of plage, which includes some pores to the north of the larger spot. The chromosphere, as imaged in  $\text{H}\alpha$  linecenter (right panel of Fig. 2), shows many almost horizontal fibrils that connect the spots to surrounding

opposite polarity pores and plage. Many of these horizontal fibrils are associated with the superpenumbra of the larger spot. These fibrils are longer (up to 20-40'') and more static than the dynamic fibrils that are the focus of this paper.

Most of the DFs are associated with the plage in the region outlined by  $x=35\text{--}60''$  and  $y=20\text{--}45''$ . The chromosphere in this region is dominated by relatively short jet-like features that appear to rise and fall within a matter of minutes. During their ascent and descent, individual DFs seem to follow the same, roughly straight, trajectory. At any given time, scores of DFs are visible in this region of interest. DFs often seem to occur in semi-coherent patches which contain several DFs at any given time. The location and orientation of these patches seems to be governed by the topology of the underlying magnetic plage region. Within such a patch, it is sometimes difficult to uniquely identify individual DFs because of the semi-coherent behavior over a few arcseconds: some of these coherent fronts show significant substructure.

The region which is dominated by DFs appears somewhat brighter in  $H\alpha$  linecenter than surrounding regions. This may be because hot coronal loops are connected to this region. Such a correlation has previously been described by De Pontieu et al. (2003b) who find a correlation between the brightness in  $H\alpha$  linecenter and that of upper transition region moss emission in Fe IX/X 171 Å (using TRACE data). Bright moss emission occurs at the footpoint regions of hot ( $> 3$  MK) coronal loops.

A full disk magnetogram taken by SOHO/MDI, centered in the middle of the time series, at 09:39 UT on 4-Oct-2005, shows that the two spots and plage in the region of interest share the same polarity (see contours of Fig. 2). Most of the associated magnetic flux seems to connect to opposite polarity to the north and west of the spots, for example the pores to the north and the plage outside the field of view to the north. This can be deduced from the potential field extrapolation shown in the left panel of Fig. 3. The field extrapolation seems to correlate reasonably well with features outlined by  $H\alpha$  in some regions, including our region of interest. However, the extrapolation deviates from the  $H\alpha$  observations in several regions of the active region to the north and east of the spots, as well as close to the pores to the north of the large sunspot.

Some DF properties vary significantly with position in the field of view. Several regions were defined: region 1 is at the edge of a plage region where the magnetic field seems more inclined (see discussion below). Region 2 covers a dense plage region (adjacent to region 1) where the fields seem more vertical. The average magnetic field strength, as derived from a full-disk MDI magnetogram (with 2'' pixels), is of order 50-100 Mx cm<sup>-2</sup> for region 1, and 150-200 Mx cm<sup>-2</sup> for region 2. The other regions contain fewer DFs and their magnetic topology is not as well defined as in regions 1 and 2. The right panel of Fig. 3 illustrates the

location of the two main regions (blue is region 1, red is region 2).

### 3. Description of Dynamic Fibrils

#### 3.1. The life of a fibril

Through visual inspection of a time lapse movie of the  $H\alpha$  linecenter images, we found many fibrils in the plage region in proximity to the two spots near the center of the image. We analyzed DFs that occurred throughout the 78 minute long time series. To analyze the properties of the DFs, we manually choose the general direction of a DF (or set of DFs). A guideline is drawn in this direction, and a subset of the data, parallel to this guideline, is extracted for further analysis. This procedure results in detailed movies of individual DFs, as well as 'xt'-plots that show the evolution of the extent of the DF along the guideline as a function of time. A total of 257 DFs were analyzed in this fashion.

In Figs. 4, 5, and 6 we present the evolution of three typical DFs. Figure 4 shows a DF in region 2. The six panels show that the DF rises rapidly to a maximum length in roughly 130 s and recedes along the same path some 260 s after first becoming visible. It is darker than its surroundings, especially at maximum extension, and seems to follow a straight path in the direction that is shared by all surrounding features. The DF has some internal structure, most clearly visible at  $t = 139$  s and  $t = 186$  s. The maximum extent is relatively modest at some  $2''$ . Despite the substructure, the DF is thin with a width of some  $0.5''$ . It is also well isolated even though a number of other DFs are visible in the immediate vicinity.

The length of the DF as a function of time is well described by a parabola, as shown in the 'xt'-plot in the top panel of Fig. 7. This is the case for the vast majority of the DFs that do not suffer from superposition and where the DF guideline was chosen with a correct angle, i.e. where the DF motion runs along the guideline. All 257 DFs used in the analysis below meet these conditions. Each individual DF is therefore fitted with a parabola and the deceleration, maximum velocity (on ascent or descent), maximum extent and duration were derived. To determine the beginning and end points of the parabola, we use the following method. The steep parabolic ascent and descent of a typical DF (and the very high cadence of our data) allows for a robust determination of the beginning and end time of each DF. The intersection (in the 'xt'-plot) between the parabolic path and a horizontal line at the beginning time or end time is used to determine the location of the "root" of the DF at, respectively, the beginning and end of its lifetime. We then use these points in the "xt"-plot to fit a parabola to the path followed by the DF.



The prevalence of parabolic paths is illustrated in all three panels of Fig. 7, where a wide variety of DFs are evident. The DF studied in this case (top panel) follows its fitted parabola very well with a constant deceleration given by  $216 \text{ m s}^{-2}$ , about two thirds of solar gravity ( $274 \text{ m s}^{-2}$ ), a maximum velocity of  $27 \text{ km s}^{-1}$ , and a maximum extent of some 1800 km. The properties for this DF and all others discussed in this paper are measured along the projected path.

An example of a much wider DF in region 2 is shown in Fig. 5. This DF has extensive internal structure and rises over a front of about  $1.5''$ , a width that is largely maintained throughout the descending phase of its relatively short lifetime of 188 s. While rising, the DF width is not constant along its axis but the DF is wider at the bottom. It is typical that such wide DFs do not rise and fall as a rigid body but rather show phase and amplitude variations in velocity at various positions away from the axis. It is also worth noting that this DF clearly becomes darker as it rises and brightens somewhat as it falls back along the same path it rose along. The 'xt'-plot in the middle panel of Fig. 7 reveals that this DF also follows a path that is very close to a parabola with a deceleration of  $286 \text{ m s}^{-2}$ , a maximum velocity of  $27 \text{ km s}^{-1}$ , and a maximum extent of 1300 km.

A longer lived DF from region 1 with a lifetime of some 290 s is shown in Fig. 6. This DF is located in a region where  $\text{H}\alpha$  images indicate that highly inclined magnetic field lines connect to the region of opposite polarity plage and pores to the west, in the top right corner of Fig. 2. The DF is wide, roughly  $1''$ , and relatively long. It is also superposed on another DF that is evident in the bottom panel of Fig. 7. Detailed examination of the movie accompanying Fig. 6 shows the separate evolution of both DFs. The superposition makes it difficult to determine whether these DFs are formed at the exact same location. Residual effects of image distortion from atmospheric seeing can cause the jagged appearance of these 'xt' profiles. Despite such distortions and the effects of superposition, a good fit for this DF can still be obtained with a deceleration of  $200 \text{ m s}^{-2}$ , a maximum velocity of  $28 \text{ km s}^{-1}$ , and a maximum extent of some 2000 km.

### 3.2. Measurements

The properties of the parabolic fits to the 'xt'-plots of 257 DFs were calculated. Visual inspection of DF time lapse movies confirmed the proper alignment of the DFs and quality of the parabolic fits.

The upper left panel of Fig. 8 shows that the DFs suffer a deceleration of on average  $146 \text{ m s}^{-2}$  with a significant spread ranging from 40 to  $320 \text{ m s}^{-2}$  and a standard deviation

of  $56 \text{ m s}^{-2}$ . This is significantly less than solar gravity. Note that the median of all DF properties is illustrated and described in the caption of Fig. 8, whereas we enumerate average values in the text. Also note that these deceleration values are twice as high as the values reported in Hansteen et al. (2006). The latter were mistakenly divided by two. The maximum DF lengths are on average 1 250 km, ranging from 400 to 5 200 km with a standard deviation of 620 km, as shown in the upper right panel of Fig. 8. The lengths found for DFs are smaller than the widely reported values of 5 000 to 10 000 km for spicules at the limb (Beckers 1968), but fit well with the values reported in De Pontieu et al. (2004). On average, the maximum velocity (on either ascent or descent) is  $18 \text{ km s}^{-1}$  ranging from 8 to  $35 \text{ km s}^{-1}$  with a standard deviation of  $6 \text{ km s}^{-1}$ , as shown in the middle left panel of Fig. 8. The maximum velocity is never observed to be lower than  $8 \text{ km s}^{-1}$ . DF durations are shown in the middle right panel of Fig. 8. The durations vary from 120 to 650 s, with an average of 290 s, and a standard deviation of 85 s. The median duration is lower at 250 s, because of the significant tail of longer duration DFs.

In addition to the parabolic fits, we have also measured DF widths. To determine the width of a DF, we calculate 'xt'-plots (with x along the direction of the guideline) for a range of locations that are each offset by one pixel in the direction perpendicular to the guideline. We then find the central axis of the DF through visual inspection of the 'xt'-plots: the location with the best-defined 'xt'-plot is chosen as the central axis. Starting at this location we find the edges of the DF in the direction perpendicular to the DF axis. We search for the two positions of maximum intensity gradient furthest from the axis where the DF is still visible in the 'xt'-plots. This is done for two different locations along the DF, at 50% and at 80% of the maximum extent for a specific time. The width is measured in this fashion at three different times in the DF lifetime, at 25%, 50% (maximum extent), and 75% of the DF duration. Although there is a large spread, we find that the widths of DFs do not vary much with height nor time. The lower left panel of Fig. 8 includes all the widths measured and shows a mean of 340 km with a standard deviation of 160 km. While the widest DF was measured to be 1100 km, most DFs have widths between the diffraction limit of 120 km and 380 km, with a significant tail of wider DFs extending to 700 km. Based on the shape of the histogram it seems likely that we are not resolving all DFs. However, a significant fraction is clearly resolved.

Visual inspection shows that the tops of most DFs are very sharply delineated (see, e.g., Fig. 7). Furthermore, inspection of 'xt'-plots shows that DFs often are outlined by a bright ring, as shown in Fig. 9. To determine how sharp the transition at the top of the DF is, we calculated the distance along the DF axis between the location of maximum intensity gradient and the location of maximum intensity in the bright ring above the DF. We refer to this measure as the thickness of the bright ring. It is unclear what causes the bright ring.

Perhaps it is related to the steep transition from chromospheric to coronal temperatures? Detailed radiative transfer calculations will be necessary to determine what causes the bright ring. Regardless of the uncertainty in interpretation, we measured the thickness of the bright ring for all 257 DFs and found an average thickness of 240 km with a standard deviation of 120 km. Over half are less than 200 km and many are unresolved, as shown in the lower right panel of Fig. 8.

### 3.3. Regional differences

Despite a large spread in properties we find clear differences between DF statistics in the two regions defined in the right panel of Fig. 3. On average, DFs in region 1 show lower decelerations, greater lengths, slightly higher maximum velocities, and longer durations than in region 2 (Fig. 8). We also found a slight tendency for DFs to be wider in region 2 (lower left panel of Fig. 8), but found no difference in transition region thickness between the two regions. Visual inspection shows that region 2 does show more DFs that are wide with significant substructure, such as the DF illustrated in Fig. 5.

To further illustrate the difference between region 1 and 2, maps of the location of DFs, color coded to show various properties, are shown in Fig. 10. As can be seen, there are clear regional differences in deceleration, duration, and length. There is a prevalence of smaller decelerations in region 1 with typical values around  $100 \text{ m s}^{-2}$ , versus roughly  $200 \text{ m s}^{-2}$  in region 2. Even more clearly, the durations in region 1 are on average about 5 minutes, whereas we find 3 minutes in region 2. Similarly, DF lengths in region 1 are typically around 2000 km, whereas shorter DFs with lengths around 1000 km dominate region 2. The spatial pattern of maximum velocities is not as clear with a large spread of velocities in both regions.

In principle some of these differences could be caused by projection effects due to the angle between the DF axis and the line of sight vector. A DF that propagates along a direction that is parallel to the direction of the line of sight would not be observed as a moving feature in these  $H\alpha$  movies. To measure the absolute extent, velocity and deceleration along the path of the DF, the line of sight needs to be perpendicular to the axis of the DF. Note that the DF durations are independent of the line of sight as they do not suffer from these projection effects.

To exclude the possibility that the regional differences in deceleration, velocity and length are caused by projection effects, we try to estimate the absolute direction of propagation of each DF. Assuming that DFs propagate along the magnetic field, their direction

can be estimated from the potential field extrapolation shown in the left panel of Fig. 3<sup>1</sup>. To estimate the effect of projection, we calculate the angle between the line of sight vector and the direction of the magnetic field at a reference height of 3 000 km above the photosphere. This height was chosen to be very roughly the sum of the top height of the quiescent chromosphere and the typical DF length. The angle between extrapolated field lines and the line of sight vector was used to correct the properties of each DF for projection.

Histograms for these corrected values are shown in Fig. 11. Not surprisingly, all corrected values are larger than the observed values. In addition, the corrected values show the same spatial differences between region 1 and 2 as the uncorrected values. To estimate how reliable the potential field extrapolation is, we measured the mismatch between the direction of the DF axis and the direction of the magnetic field as projected onto the surface, and found it to be of order 20 – 30 degrees. A mismatch of this magnitude can lead to significant errors in calculating the projection angle if the DF axis is nearly parallel to the projection of the line of sight vector onto the surface. This means that the corrected values should be considered with caution, especially since the calculations are also based on various assumptions whose validity is unclear. The poor resolution of the MDI magnetogram, the possible non-potentiality of the active region, and the uncertainty in the actual DF height with respect to the chosen reference height, all could lead to significant errors in the estimated projection angle. For example, the potential field extrapolation clearly fails in the top part of region 1 where nearly horizontal fields are predicted. Such horizontal fields are incompatible with the visual appearance of  $H\alpha$  linecenter images. In addition, since horizontal fields at this location are almost parallel to the line of sight vector, they lead to very large and obviously erroneous corrections of the local DF parameters.

Despite these reservations, it is very difficult to conceive of a magnetic topology with an orientation to the line of sight that would remove the regional differences for all derived parameters. In addition, the regional differences in duration (which are independent of projection effects) as well as the correlations found between various parameters in the following subsection, strongly suggest that regional differences are not caused by projection effects.

### 3.4. Correlations

Scatterplots of various DF properties reveal intriguing correlations. The most striking correlation, also presented in Hansteen et al. (2006), is that between the deceleration and

---

<sup>1</sup>See <http://zorak.lmsal.com/bdp/projects/vrml/spic.vrml> for a VRML representation. The straight red line in the VRML link is parallel to the line of sight.

the maximum velocity of the DFs, in which a linear relationship is evident (upper left panel of Fig. 12). The larger the deceleration the DF suffers from, the higher the maximum (initial or final) velocity it shows. Note that there are, again, significant differences between region 1 and 2: the DFs in region 2 typically have larger decelerations for a given maximum velocity. A linear fit to the observed relationship between the deceleration and velocity shows that both regions have almost identical slopes.

Another interesting correlation is that between the maximum length and the duration of a DF (upper right panel of Fig. 12). The longer DFs tend to have longer lifetimes. As expected from the histograms in the upper and middle right panels of Fig. 8, the DFs in region 1 gravitate towards the upper right of this scatterplot. We also find that the maximum velocity and maximum length of DFs is well correlated (lower right panel of Fig. 12): DFs with higher maximum velocity tend to be longer. However, there is a difference in the slope in regions 1 and 2. A linear fit for region 1 reveals a slope of 87 km per km s<sup>-1</sup>, and 60 km per km s<sup>-1</sup> for region 2. DFs in region 1 are longer for the same maximum velocity.

The deceleration of DFs shows a somewhat less clear correlation with the DF duration (lower left panel of Fig. 12). The longest-lived DFs typically suffer from the lowest deceleration. This correlation shows a large spread, and is not quite linear for the total population of DFs. It seems that each region may have its own linear relationship. DFs in region 1 show a more steep dependence of duration on deceleration, whereas those in region 2 show a smaller range of durations, for a range of decelerations that is similar in extent to that of region 1.

Based on the correlations described in the above, one would perhaps also expect a correlation between the deceleration and maximum length, or between the maximum velocity and duration. However, such correlations are not clear from the observations, as demonstrated in Fig. 13. The large scatter and different slopes that are evident in the plots that do show correlations may be partially responsible for the lack of clear correlation between deceleration and maximum length or the maximum velocity and duration. However, it is also clear that there are very significant regional differences in Fig. 13, with each region occupying a different area in the scatterplots, and in some cases showing different slopes. It seems probable that such regional differences also are responsible for the lack of clear correlations.

When we take the line-of-sight correction into account, none of these correlations, or the lack of correlation, change qualitatively. Evidently, the correlation between deceleration and velocity, or that between maximum velocity and length cannot change significantly because of projection effects, since both parameters would be corrected by the same factor. The fact that the other correlations, between duration on the one hand, and either deceleration, length or velocity, do not change qualitatively indicates that projection effects do not dominate our

dataset.

The same arguments also apply to any kind of selection effects that are caused by the fact that DFs with very large line-of-sight velocities could disappear from or be invisible in our relatively narrow (128 mÅ) H $\alpha$  linecenter bandpass. Since DFs are much wider spectral features (with widths of order 1000 mÅ, see, e.g. Beckers 1968) than the width of the bandpass, this means that only features with line-of-sight velocities of order 20 or more km/s would be invisible or only partially visible in the linecenter timeseries. While in a few cases we can see some fading of the DF during its descent, it is still possible to trace the top of the DF to its end point. Given these arguments, the passband effect can only change the derived correlations marginally.

Note that all of the measurements on which the correlations are based, depend on the identification of a single DF rising above the chromospheric background. The latter can be quite noisy and sometimes less well defined. Filtergrams taken in the wings of H $\alpha$  might be helpful for a more exact determination of the root location of each DF, but such filtergrams were unavailable in this dataset. This means that the measured length and maximum velocity could in fact be somewhat higher than reported here. However, given the rapid rise and fall of DFs, the measured duration is quite insensitive to this effect. Since we are measuring the acceleration by fitting parabolas to the height profile, the acceleration is also insensitive to the position of the chromospheric background. Overall, this implies that the relative uncertainty in determining the roots of DFs are unlikely to qualitatively change the correlations reported here.

The interpretation of these correlations, or the lack thereof, will be discussed at length in §4.

### 3.5. Oscillations

The regional differences in DF durations evident in the middle right panel of Fig. 8, with 3 minute lifetimes dominating region 2 and lifetimes around 5 minutes more dominant in region 1, suggest a role for chromospheric waves or oscillations in the formation mechanism of DFs. Oscillations in the chromosphere are typically not steady harmonic waves, but wave trains of finite duration. For this reason we perform a wavelet analysis of the H $\alpha$  data, since it allows for localization in time of periodic signals. The mother wavelet we use is the complex valued Morlet wavelet ( $k = 6$ ) which consists of a plane wave modulated by a Gaussian, an appropriate shape for wave trains. To estimate the statistical significance of the wavelet power spectra (95 % confidence interval), we compare them to theoretical spectra for

white noise, following Torrence & Compo (1998) and De Moortel & Hood (2000). Taking into account the cone of influence (Torrence & Compo 1998), we calculate for each superpixel the number of wavepackets in the  $H\alpha$  timeseries for which the wavelet power is significant. This is done for a range of wave periods from 150 to 600 seconds. A superpixel is defined as the average of  $4 \times 4$  original  $0.063''$  pixels. Note that the original data is oversampled by a factor of almost 3 with respect to the diffraction limit (120 km) of the SST at the wavelength of  $H\alpha$ .

The upper left and upper right panels of Fig. 14 show, for each location of the lower left panel, the number of significant wavepackets (during the  $H\alpha$  timeseries) for waves with a period of 180 s and 300 s respectively. The lower right panel shows which wave period dominates, i.e., has the most wavepackets, at each location of the field of view. From this figure, we find that many locations show significant oscillatory power throughout the timeseries. The dominant period of this power varies across the field of view. Clearly visible are the dominant 3 minute oscillations in the sunspots around  $x=27''$  and  $y=37''$  and at  $x=45''$  and  $y=15''$ . In addition, the dense plage region which we have designated as region 2, shows a preponderance of 3 minute oscillations. In contrast, region 1, adjacent to the dense plage region, is dominated by oscillations with long periods around and above 5 minutes. In this region, the magnetic field is more inclined than in the dense plage region. The longer, less dynamic and more horizontal fibrils, such as those in the superpenumbra of both spots, seem to be dominated by oscillations with periods longer than 10 minutes.

It is interesting to note that the dominant period in region 2 corresponds exactly to the DF duration we observe in region 2. Apparently, DFs typically live for about 3 minutes in this region, which is also the dominant periodicity of the oscillations. Likewise, region 1 is dominated by 5 minute oscillations, and contains DFs with lifetimes of order 5 minutes. Since the oscillation measurements are based on the same data, it seems clear that some DFs are periodic or recurring. This was also described by Hansteen et al. (2006) and suggests a relationship between chromospheric waves and DFs, which will be further explored in §4.

## 4. Discussion

### 4.1. Observational Findings

Most DFs follow parabolic paths with a symmetrical ascending and descending phase. These paths are characterized by a large initial velocity, usually of order  $15\text{--}20 \text{ km s}^{-1}$  (middle left panel of Fig. 8), that decreases linearly with time until the DF has retreated completely. At the end of its life, a DF's downward velocity is roughly identical to the initial upward

velocity. The linear decrease with time of the velocity, i.e., the deceleration, is usually between 120 and 280  $\text{m s}^{-2}$  (upper left panel of Fig. 8). There is a clear linear relationship between the deceleration and the maximum (down- or upward) velocity of the DF (upper left panel of Fig. 12).

DFs reach maximum lengths of order 1,000 to 2,000 km (upper right panel of Fig. 8) during their lifetimes of 3 to 8 minutes (middle right panel of Fig. 8). The duration and maximum length are well correlated (upper right panel of Fig. 12), which indicates that uncertainty about the line-of-sight correction may not play an important role in the regional differences we find. We resolve more than half of the DFs we observe. The average thickness is 240 km (lower left panel of Fig. 8), with a range between the diffraction limit (120 km) and 1000 km. Some DFs occur over a wider spatial area, whereas others are very thin and stay thin throughout their lifetime. Many of the wider DFs have variable widths as a function of time. These give the visual appearance of a wave front with varying phase speeds or amplitude in the direction perpendicular to the DF axis. There is often a brightening above the DF, which can be clearly seen in 'xt'-plots (Fig. 9). This brightening might be a sign of increased temperatures at the top of the DF. The thickness of this transition is not resolved and is less than 120 km in more than half of the DFs studied (lower right panel of Fig. 8).

DFs have significantly different properties in two regions within our field of view. Region 2 contains dense plage, i.e., a collection of strong magnetic field concentrations in which the magnetic field is generally more vertical. Region 1 is located at the edge of this dense plage region, where the magnetic field is more inclined, as it connects to relatively nearby opposite polarity plage. The DFs in the dense plage region are shorter ( $\sim 1,000$  km), have higher decelerations ( $\sim 200 \text{ m s}^{-2}$ ), slightly lower velocities ( $\sim 15 \text{ km s}^{-1}$ ) and shorter durations of about 3 minutes (Figs. 8 and 10). In contrast, the DFs in the region where the field is more inclined are longer ( $\sim 2,000$  km), have lower decelerations ( $\sim 120 \text{ m s}^{-2}$ ), slightly higher velocities ( $\sim 20 \text{ km s}^{-1}$ ) and longer durations of about 5 minutes (Figs. 8 and 10). In addition, DF lifetimes correlate well with the dominant periodicities observed in both regions: 3 minute oscillations dominate  $\text{H}\alpha$  in the dense plage region, whereas 5 minute oscillations dominate in the region with more inclined field (Fig. 14).

## 4.2. Interpretation

Our measurements of DFs and oscillatory power strongly suggest that chromospheric waves drive DFs upward. These chromospheric waves are generated by convective flows and (global) oscillations in the photosphere and convection zone. The magnetic field concentrations provide a channel for these disturbances to propagate up through the chromosphere.



During their path upwards, they shock and drive chromospheric plasma upwards, forming DFs in the process. This mechanism was originally suggested in rudimentary form by Parker (1964). Some models have further studied the effects of the convective part of the photospheric driver on the chromosphere in the so-called rebound-shock model (Hollweg 1982; Sterling & Hollweg 1989; Sterling & Mariska 1990). More recently, De Pontieu et al. (2004) included both the convective driver and global oscillations in varying magnetic topologies to directly describe their (lower resolution) observations of dynamic fibrils. The latter model’s predictions agree well with the current findings.

This scenario is confirmed by analysis of advanced numerical simulations (see Hansteen et al. (2006) and next subsection) in which dynamic fibril-like features with properties identical to those in our data occur. From the simulations, it is clear that the observed parabolic paths indicate that DFs are shock driven. When a shock hits the transition region (i.e, the top of a DF), the transition region is catapulted upwards at a velocity that exceeds the sound speed in the chromosphere ( $\sim 10 \text{ km s}^{-1}$ ). Shock waves generally have velocity profiles in the form of ‘N’- or ‘sawtooth’ shapes (e.g. Mihalas & Mihalas 1984). Thus, a plasma parcel passing through a shock wave will first experience a sudden kick in velocity — the shock itself — and thereafter a gradual linear deceleration as the shock recedes. Assuming a shock wave with amplitude or shock strength of  $u_0$  and linear deceleration  $a$

$$u(t) = -at + u_0,$$

it is trivially verified that a plasma parcel passing through the shock will describe a parabolic path; integrating gives a parcel position that moves as

$$\xi(t) = -\frac{1}{2}at^2 + u_0t + \xi_0.$$

DF formation from chromospheric shocks is compatible with the fact that we do not find any DFs with initial (maximum) velocities of less than  $10 \text{ km s}^{-1}$ . Waves with smaller amplitudes will not form shocks and hence DFs. The observed lower limit to the maximum velocities provides an estimate of the sound speed in the upper chromosphere ( $10 \text{ km s}^{-1}$ ). Its value is compatible with chromospheric temperatures from solar models. More generally, the observed maximum velocities provide a robust estimate of the Mach number of chromospheric shocks. Our observations indicate that shocks with Mach numbers of 1 through at least 3.5 are ubiquitous in the magnetized chromosphere, and drive DFs.

Analysis of numerical simulations (Hansteen et al. 2006) further shows that several different effects influence the shock formation and evolution so that the observed correlations (e.g., between deceleration and velocity) and regional differences follow naturally.

The oscillatory power spectrum of the photospheric driver is dominated by power at 5 minutes. The chromosphere acts as a filter to the input from below, filtering out waves

with periods that are longer than the local acoustic cutoff period. In general, the acoustic cutoff period depends on the inclination of the magnetic field lines to the vertical (Suematsu 1990; De Pontieu et al. 2004). Under conditions of vertical magnetic field (e.g., region 2), this means that the chromosphere is dominated by oscillations and waves with periods at the acoustic cutoff of 3 minutes. As a result, the DFs formed in the dense plage of region 2 are driven by shocks with periods of 3 minutes and thus have lifetimes of order 3 minutes. In contrast, the inclined field, such as that found in region 1, increases the acoustic cutoff period. This allows the photospheric waves with periods of 5 minutes to leak into the chromosphere, develop into shocks and form DFs with similar lifetimes.

Since most of the oscillatory power in the photosphere occurs for periods of 5 minutes, the driver in inclined field regions is generally stronger than in regions with more vertical field. This effect is enhanced by the fact that, in dense plage regions, the amplitude of convective flows and global oscillations is generally reduced at the photospheric level. DFs that form along inclined field lines also experience only the component of gravity along the magnetic field, so that decelerations are generally lower in the inclined field region.

The observed correlation between deceleration and maximum velocity can be understood in terms of shock wave physics and the fact that DFs are driven by single shocks. For a given wave period, 'N'-shaped shock waves will show a steeper decline with time in velocity for a greater shock strength. In other words, DFs with higher maximum velocity, i.e., those that are driven by stronger shocks, will show greater deceleration, for a given DF lifetime.

It is the combination of these effects that explains the observed regional differences and correlations. Region 2 contains more vertical field, so that only 3 minute power drives the chromospheric waves and shocks. Given the photospheric power spectrum and the reduced power in dense plage regions, this leads to lower amplitudes, i.e., lower maximum velocity. In addition, the short lifetimes and more vertical field lead to higher decelerations, and shorter lengths. Conversely, region 1 contains more inclined field, allowing the full photospheric peak power at 5 minutes to leak into the chromosphere to drive DFs. As a result, the velocity amplitude is greater, and the longer lifetimes and less vertical field lead to lower decelerations and longer lengths.

### 4.3. Numerical Simulations

These findings are confirmed when comparing the observations with recent advanced numerical radiative MHD simulations that include the convection zone, photosphere, chromosphere, transition region and corona (Hansteen et al. 2006). The equations of MHD

are solved using an extended version of the numerical code described in Dorch & Nordlund (1998); Mackay & Galsgaard (2001) and in more detail by Nordlund & Galsgaard at <http://www.astro.ku>. The code functions by using a sixth order accurate scheme to determine partial spatial derivatives. The equations are stepped forward in time using the explicit 3rd order predictor-corrector procedure by Hyman (1979), modified for variable time steps. In order to suppress numerical noise, high-order artificial diffusion is added both in the forms of a viscosity and in the form of a magnetic diffusivity. Thermal conduction along the magnetic field in the corona and transition region is treated by operator splitting and using a multi-grid solver. The radiative flux divergence from the photosphere and lower chromosphere is obtained using the method of Nordlund (1982) based on group mean opacities as modified by Skartlien (2000) to account for scattering. For the upper chromosphere, transition region and corona we assume effectively thin radiative losses. For the middle and upper chromosphere we parametrize the optically thick radiative losses in strong lines and continua from hydrogen and singly ionized calcium by using escape probabilities calculated in 1D with the code of Carlsson & Stein (1992, 1994, 1995, 1997, 2002). Further description of the 3D code may be found in Hansteen & Gudiksen (2005).

The 2d simulations described here are run on a grid of  $512 \times 150$  points spanning  $16 \times 12 \text{ Mm}^2$ . In height, these models cover a region from 2 Mm below to 10 Mm above the photosphere. The grid has uneven spacing in the vertical,  $z$ , direction with a grid size of 30 km in the photosphere and chromosphere becoming gradually larger in the corona. We have also run 2d calculations on coarser grids of  $256 \times 150$  and  $128 \times 150$  points, as well as 3d runs of  $128 \times 64 \times 150$  points spanning  $16 \times 8 \times 12 \text{ Mm}^3$ , with results similar to those reported here.

At the start of a given simulation, a potential magnetic field is added to a model of the solar atmosphere. The resultant model is then allowed to evolve in time until a quasi-steady state is achieved. This takes on the order of a half hour solar time. The models are convectively unstable due the radiative losses in the photosphere. This results in a temperature structure similar to that derived in semi-empirical solar models. The average temperature at the bottom boundary is maintained by setting the entropy of the fluid entering the computational domain. The bottom boundary, based on characteristic extrapolation, is otherwise open, allowing fluid to enter and leave the computational domain as required. The magnetic field at the lower boundary is advected with the fluid. To prevent coronal cooling the upper temperature boundary is set to evolve towards a temperature of 800 000 K on a timescale of 10 – 100 s. (In the 3d models coronal temperatures are maintained by self consistent magnetic dissipation.) A snapshot of the temperature structure in the lower part of the model including the convection zone, photosphere, and chromosphere is shown in Fig. 15.

Waves generated by convection propagate through the chromosphere, steepen and form shocks roughly 1 Mm above the photosphere. In regions above the level where plasma  $\beta = 1$  the propagation is modified by the magnetic field and the waves are subjected to reflection, refraction and mode coupling as described by Bogdan et al. (2003). Of interest to us here are the shocks that propagate along field lines that enter the coronal plasma as indicated in Fig 15. These shocks lift and accelerate the transition region as they propagate into the corona. Plotting the motion of the transition region along one such field line as a function of time, e.g. a 'xt' plot, reveals that the position of the transition region describes a parabola (Fig. 16, compare with Fig. 7). In the left panel of Fig. 16 the logarithm of the temperature is shown, the right panel shows the velocity. It is worth noting that except for a brief moment in the early ascending phase the simulated DF shows both upflowing and downflowing velocities along its length at a given time. During descent, the DF has only downflowing plasma. Note also that near its base the simulated DF shows downflows for a major portion of its lifetime.

We have measured the transition region motion along several field lines in several 'DF-like' events and fitted the motion with parabolas. The resulting correlation between measured maximum velocities and decelerations (Fig. 17) show the same trend as found in the observed DFs (upper left panel of Fig. 12): large decelerations are correlated with large maximum velocities. The range in maximal velocities and decelerations is approximately the same as that found in the observed DFs, and the slope in the correlation is about the same. Inspection of Fig. 16 also indicates that the simulated DFs have the same range of heights and durations that the observed DFs display.

Higher resolution 3D simulations with varying magnetic topologies will be necessary to explain the range of DF widths, the internal DF substructure, and what determines the sometimes sheet-like structure of some DFs. Such simulations will also help to fully explain the range of periods and lifetimes that we observe.

#### 4.4. Quiet Sun equivalents

How do these findings relate to quiet Sun phenomena such as mottles and spicules at the limb? There are many similarities between mottles and DFs. Both phenomena appear as highly dynamic, dark features in the wings and core of  $H\alpha$ . They are associated with magnetic flux concentrations that can be observed as bright points in the blue wing of  $H\alpha$ . More importantly, like DFs, mottles also follow parabolic paths. In an excellent analysis of the dynamics of inclined mottles (which they refer to as disk spicules) Suematsu et al. (1995) find that:

- mottles seem to be generated several hundred kilometers above the photosphere,
- mottles undergo real mass motion of order  $10\text{-}30 \text{ km s}^{-1}$ , extending up to  $2\text{-}10 \text{ Mm}$  during their lifetime of  $2\text{-}15$  minutes,
- most mottles are observed to ascend and descend,
- mottles in weak plage, or the interior of network cells are more vertical and shorter than the more inclined quiet Sun mottles,
- the appearance of mottles is varied, they can be thick, thin, tapered or not, curved or straight,
- some mottles show downward motion close to their base during the ascending phase,
- the decelerations observed in mottles are too small to be consistent with a purely ballistic flight (at solar gravity) and the observed Doppler shifts,
- the largest doppler signal appears at the beginning of the ascending phase, and at the end of receding phase,
- the observed velocity profiles are compatible with impulsive acceleration and constant deceleration afterward.
- the maximum upward velocity is usually identical in amplitude to the maximum downward velocity,
- there is a linear relationship between the duration and the maximum length of mottles,
- there is a correlation between the average velocity and maximum length,
- nearby mottles are often found to be driven by a common disturbance.

These findings agree strikingly well with our observations and modelling of DFs, with only a few discrepancies. The lifetimes and maximum lengths of the mottles Suematsu et al. (1995) analyzed are typically longer than those of the DFs we describe. We believe this is in part a selection effect, as we chose to focus only on highly dynamic and shorter features in our dataset. We note that our dataset also contains a large number of highly inclined fibrils that are longer lived and less dynamic than the DFs (see, e.g., Fig. 14). In addition, preliminary analysis of high-quality SST data of quiet Sun mottles indicates that the most inclined mottles are on average longer, but that many of the mottles actually show lengths ( $1,000\text{-}5,000 \text{ km}$ ) that are similar to those of DFs. Until further detailed analysis,

it can however not be excluded that DFs associated with plage are on average somewhat shorter in length and lifetime than quiet Sun mottles. Preliminary analysis of our numerical simulations suggests that these differences could be related to large scale differences in magnetic topology. Further work is necessary to establish the exact relationship between mottles and DFs. However, it should be noted that in addition to these striking similarities with mottles, recent observations of limb spicules (Christopoulou et al. 2001) show clear parabolic paths with decelerations and maximum velocities of the same order as those reported for mottles (Suematsu et al. 1995) and those we find for DFs. Older observations of limb spicules have also shown evidence for correlations between velocities and maximum lengths (Rush & Roberts 1953), and between duration and height (Dizer 1953). These correlations are similar to the ones we find for DFs. In addition, Lippincott (1957) has reported on collective behavior of spicules or mottles over several thousand kilometers.

As discussed also by Hansteen et al. (2006), these similarities strongly suggest that chromospheric shock waves cause significant excursions of the upper chromosphere in both active region and quiet Sun. Such a scenario was proposed by De Pontieu et al. (2004) using SST and TRACE data. Further detailed analysis of our numerical simulations can help shed light on several unresolved issues, such as the role of reconnection in forming quiet Sun jets, or whether the observed height of limb spicules can be explained by the mechanism proposed here.

Hansteen et al. (2006) suggest that it is possible that limb spicules consist of two populations: jets that are driven by shocks (as described in this paper), and jets caused by reconnection. The latter jets could form a subset that on average is taller than the shock driven jets, and perhaps be a part of a continuous spectrum of reconnection jets that includes surges, macrospicules and  $H\alpha$  upflow events (Chae et al. 1998). These taller jets may be the features that have UV counterparts (e.g, observed by SUMER), which Wilhelm (2000) calls “spicules”.

## 5. Summary

The combination of high-resolution chromospheric data and advanced numerical simulations strongly suggests that DFs are formed by upwardly propagating chromospheric oscillations/waves. These waves are generated in the convection zone/photosphere as a result of global p-mode oscillations and convective flows. The magnetic topology acts as a filter, so that only waves of certain periods can propagate into and through the chromosphere, forming shocks along the way, up to regions where  $H\alpha$  is formed.

Some of the key observational/modelling results on which this interpretation is based are:

- DFs follow a parabolic path
- DFs in dense plage regions are shorter, slower, undergo larger deceleration and live shorter
- DFs in regions adjacent to dense plage regions are longer, faster, undergo less deceleration, and live longer
- DFs in dense plage regions show periodicities around 180 s
- DFs in regions adjacent to dense plage regions show periodicities around 300 s
- the velocity and deceleration of all DFs is well correlated: the higher the velocity, the more deceleration
- this correlation is reproduced well in numerical simulations where DFs are driven by shocks caused by upward propagating waves in the chromosphere.
- DFs in the simulations follow parabolic paths as well.
- the simulations reproduce the observed values of maximum velocities, decelerations and lengths well.

From the results describe above and by Hansteen et al. (2006), it seems clear that in active regions, most dynamic fibrils are formed by chromospheric shocks driven by convective flows and oscillations in the photosphere.

BDP was supported by NASA grants NAG5-11917, NNG04-GC08G and NAS5-38099 (TRACE), and thanks the ITA/Oslo group for excellent hospitality. VHH thanks LMSAL for excellent hospitality during the spring of 2006. This research was supported by the European Community’s Human Potential Programme through the European Solar Magnetism Network (ESMN, contract HPRN-CT-2002-00313) and the Theory, Observation and Simulation of Turbulence in Space (TOSTISP, contract HPRN-CT-2002-00310) programs, by The Research Council of Norway through grant 146467/420 and through grants of computing time from the Programme for Supercomputing. The Swedish 1-m Solar Telescope is operated on the island of La Palma by the Institute for Solar Physics of the Royal Swedish Academy of Sciences in the Spanish Observatorio del Roque de los Muchachos of the Instituto de Astrofísica de Canarias. The authors thank K. Schrijver and M. DeRosa for useful discussions and comments.

## REFERENCES

- Al, N., Bendlin, C., Hirzberger, J., Kneer, F., & Trujillo Bueno, J. 2004, A&A, 418, 1131
- Beckers, J. M. 1968, Sol. Phys., 3, 367
- Bogdan, T. J. et al. 2003, Ap. J., 599, 626
- Carlsson, M., & Stein, R. F. 1992, Ap. J.l, 397, L59
- Carlsson, M., & Stein, R. F. 1994, in Chromospheric Dynamics, ed. M. Carlsson, 47–+
- . 1995, Ap. J.l, 440, L29
- . 1997, Ap. J., 481, 500
- . 2002, Ap. J., 572, 626
- Chae, J., Wang, H., Lee, C.-Y., Goode, P. R., & Schuhle, U. 1998, Ap. J.l, 504, L123+
- Christopoulou, E. B., Georgakilas, A. A., & Koutchmy, S. 2001, Sol. Phys., 199, 61
- De Moortel, I., & Hood, A. W. 2000, A&A, 363, 269
- De Pontieu, B., Berger, T. E., Schrijver, C. J., & Title, A. M. 1999, Sol. Phys., 190, 419
- De Pontieu, B., & Erdélyi, R. 2006, Royal Society of London Philosophical Transactions Series A, 364, 383
- De Pontieu, B., Erdélyi, R., & De Moortel, I. 2005, Ap. J.l, 624, L61
- De Pontieu, B., Erdélyi, R., & de Wijn, A. G. 2003a, Ap. J.l, 595, L63
- De Pontieu, B., Erdélyi, R., & James, S. P. 2004, Nature, 430, 536
- De Pontieu, B., Tarbell, T., & Erdélyi, R. 2003b, Ap. J., 590, 502
- Dizer, M. 1953, Compt. Rend., 235, 1016
- Dorch, S. B. F., & Nordlund, A. 1998, A&A, 338, 329
- Grossmann-Doerth, U., & Schmidt, W. 1992, A&A, 264, 236
- Handy, B. N. et al. 1999, Sol. Phys., 187, 229
- Hansteen, V. H., De Pontieu, B., van Noort, M., Rouppe van der Voort, L., & Carlsson, M. 2006, submitted to ApJ letters



- Hansteen, V. H., & Gudiksen, B. 2005, in *Connecting Sun and Heliosphere, Proceedings of the Conference Solar Wind 11 – SOHO 16 12–17 June 2005*, ed. B. Fleck & T. Zurbuchen, 483–486
- Hollweg, J. V. 1982, *Ap. J.*, 257, 345
- Hyman, J. 1979, in *Adv. in Comp. Meth. for PDE's—III*, ed. R. Vichnevetsky & R. Stepleman, 313
- Kulidzanishvili, V. I., & Nikolskii, G. M. 1978, *Sol. Phys.*, 59, 21
- Lippincott, S. L. 1957, *Smithsonian Contributions to Astrophysics*, 2, 15
- Mackay, D. H., & Galsgaard, K. 2001, *Sol. Phys.*, 198, 289
- Mihalas, D., & Mihalas, B. W. 1984, *Foundations of Radiation Hydrodynamics* (New York: Oxford University Press)
- Nishikawa, T. 1988, *PASJ*, 40, 613
- Nordlund, Å. 1982, *A&A*, 107, 1
- Parker, E. N. 1964, *Ap. J.*, 140, 1170
- Platov, J. V., & Shilova, N. S. 1971, *Sol. Phys.*, 19, 52
- Rush, J. H., & Roberts, W. O. 1953, *Astron. J.*, 58, 226
- Scharmer, G. B., Bjelksjö, K., Korhonen, T. K., Lindberg, B., & Petterson, B. 2003a, in *Innovative Telescopes and Instrumentation for Solar Astrophysics*. eds. S.L. Keil & S.V. Avakyan. *Proc. SPIE.*, Vol. 4853, 341–350
- Scharmer, G. B., Dettori, P. M., Löfdahl, M. G., & Shand, M. 2003b, in *Innovative Telescopes and Instrumentation for Solar Astrophysics*. eds. S.L. Keil & S.V. Avakyan. *Proc. SPIE.*, Vol. 4853, 370–380
- Skartlien, R. 2000, *Ap. J.*, 536, 465
- Sterling, A. C. 2000, *Sol. Phys.*, 196, 79
- Sterling, A. C., & Hollweg, J. V. 1989, *Ap. J.*, 343, 985
- Sterling, A. C., & Mariska, J. T. 1990, *Ap. J.*, 349, 647
- Suematsu, Y. 1990, *LNP Vol. 367: Progress of Seismology of the Sun and Stars*, 367, 211

- Suematsu, Y., Wang, H., & Zirin, H. 1995, *Ap. J.*, 450, 411
- Title, & Rosenberg. 1981, *Optical Engineering*, 20, 815
- Torrence, C., & Compo, G. P. 1998, *Bulletin of the American Meteorological Society*, vol. 79, Issue 1, pp.61-78, 79, 61
- Tsiropoula, G., Alissandrakis, C. E., & Schmieder, B. 1994, *A&A*, 290, 285
- Tsiropoula, G., & Tziotziou, K. 2004, *A&A*, 424, 279
- Tziotziou, K., Tsiropoula, G., & Mein, P. 2003, *A&A*, 402, 361
- . 2004, *A&A*, 423, 1133
- van Noort, M., & Rouppe van der Voort, L. 2006, submitted to *ApJ Letters*
- van Noort, M., Rouppe van der Voort, L., & Löfdahl, M. G. 2005, *Sol. Phys.*, 228, 191
- Wilhelm, K. 2000, *A&A*, 360, 351

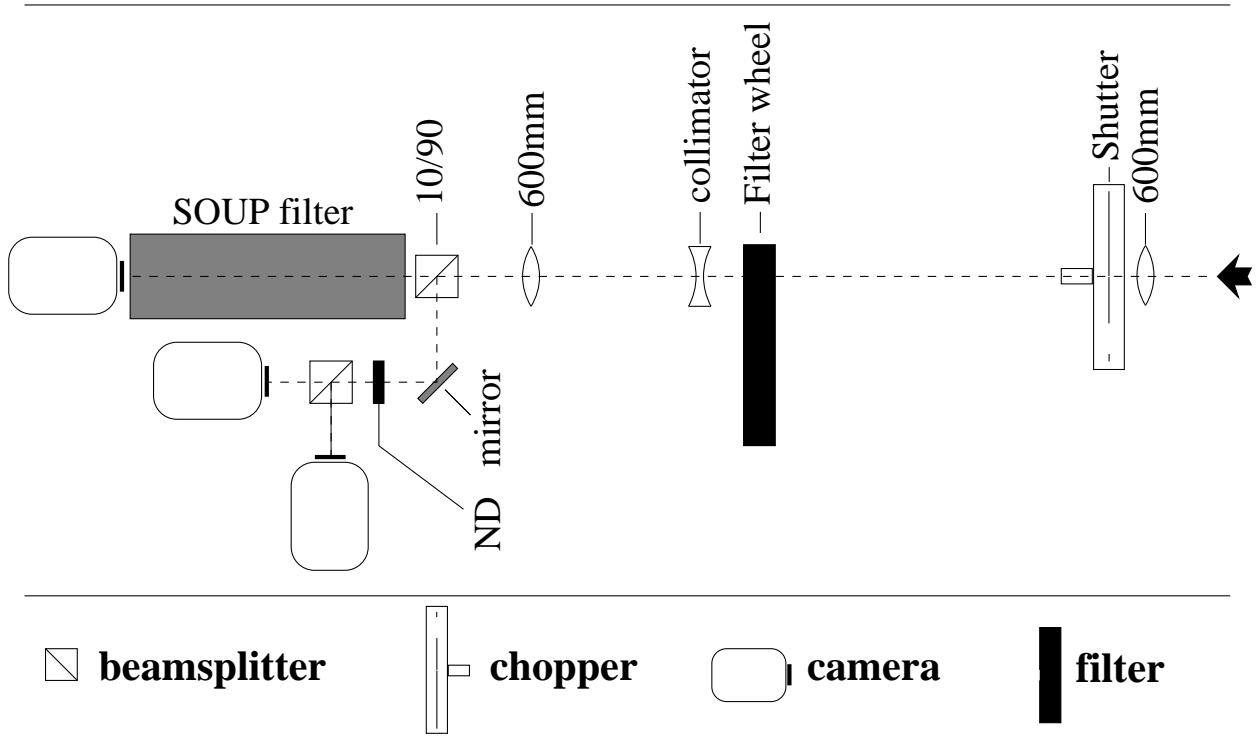


Fig. 1.— Optical setup at the Swedish 1 m Solar Telescope (SST) in La Palma used to obtain  $H\alpha$  data on 4-Oct-2005. See §2 for details.

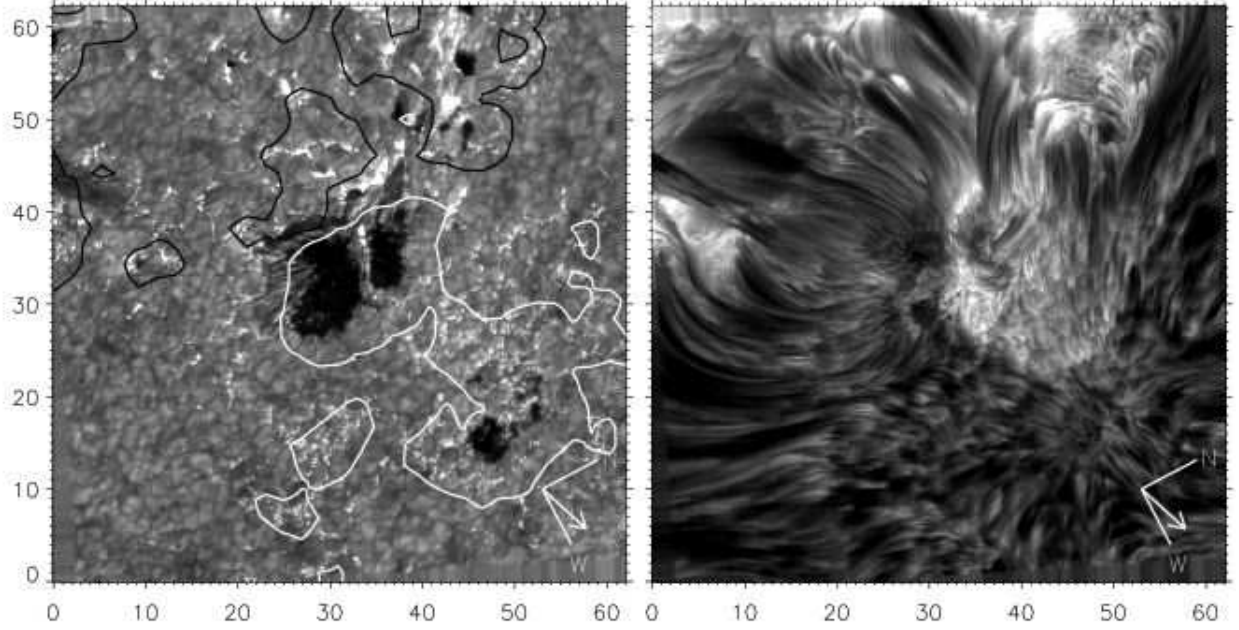


Fig. 2.— Images taken in  $H\alpha$  wideband (left panel) and  $H\alpha$  linecenter (right panel) of part of NOAA AR 10813 taken at SST on 4-Oct-2005. Tickmarks are in arcseconds. The dynamic fibrils (DFs) are predominantly observed in the mostly unipolar plage region between the two sunspots, for  $x=35-60''$  and  $y=20-40''$ . The white and black contours in the left panel outline the positive and negative magnetic flux from a full-disk MDI magnetogram. The active region is located at heliocentric coordinates S7, E37. The direction of disk center is indicated by a white straight arrow. An mpeg-movie showing the temporal evolution of dynamic fibrils (DFs) in  $H\alpha$  linecenter is available online.

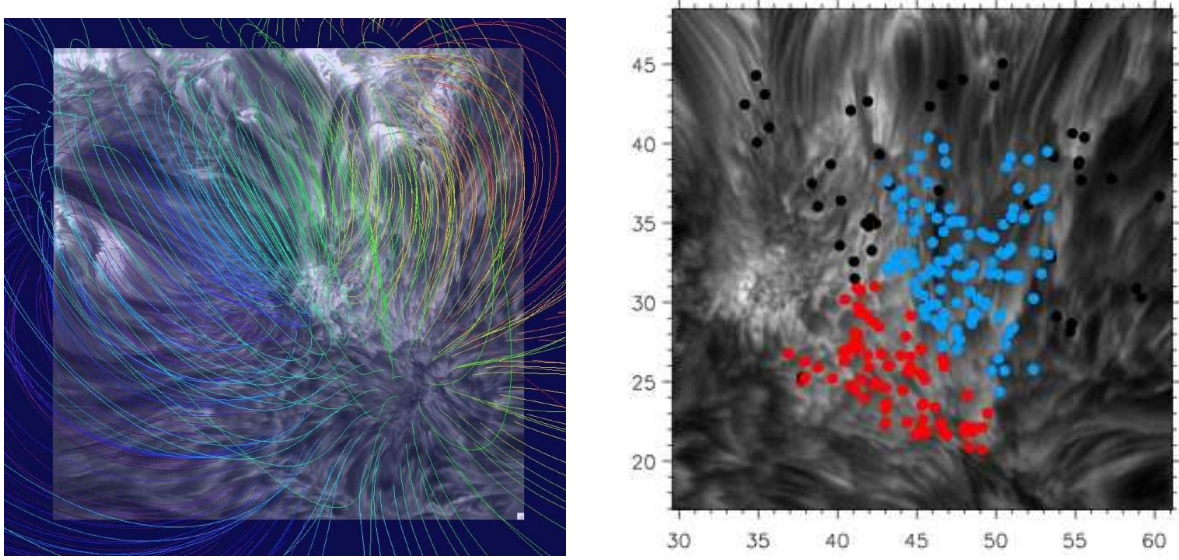


Fig. 3.— Left panel shows a potential field extrapolation superposed on a  $H\alpha$  linecenter image. The potential field extrapolation is based on a full-disk MDI magnetogram in the middle of the time series. Colors of fieldlines are only chosen for clarity. Right panel shows a  $H\alpha$  linecenter image with positions of DFs overplotted. Blue dots indicate DFs located in region 1, whereas red dots indicate DFs located in region 2. All other DFs that were measured are shown as black dots. Region 2 is the site of a dense plage area where magnetic fields are more concentrated and more vertical. Region 1 is adjacent to this dense plage region. Magnetic fields here are more inclined as the field connects to the opposite polarity plage that surrounds the pores at the top of Fig. 2.

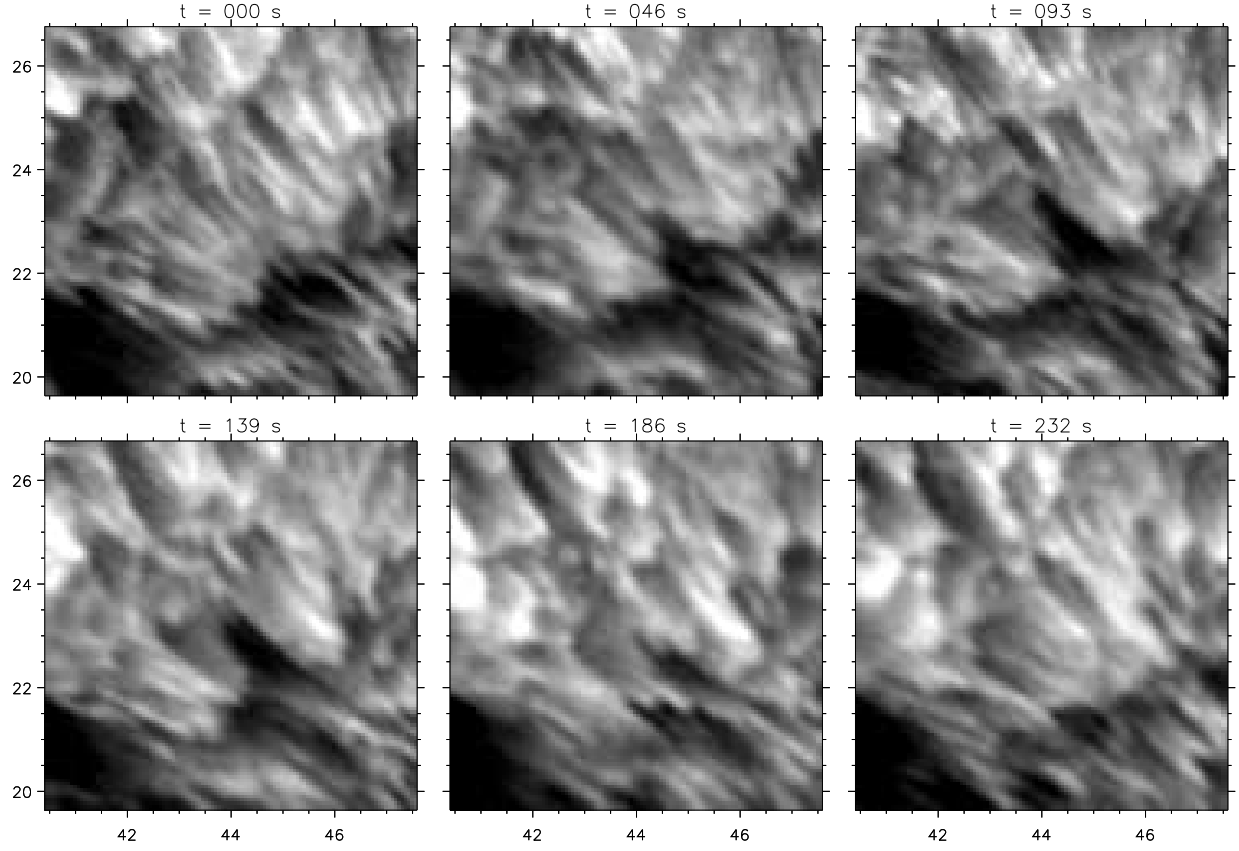


Fig. 4.— Snapshots in H $\alpha$  linecenter that show the temporal evolution of a dynamic fibril as it rises and retreats. This DF is thin, short and highly dynamic. It shows some evidence of substructure during its evolution. It is located in region 2. An mpeg-movie showing the temporal evolution of this DF is available online.

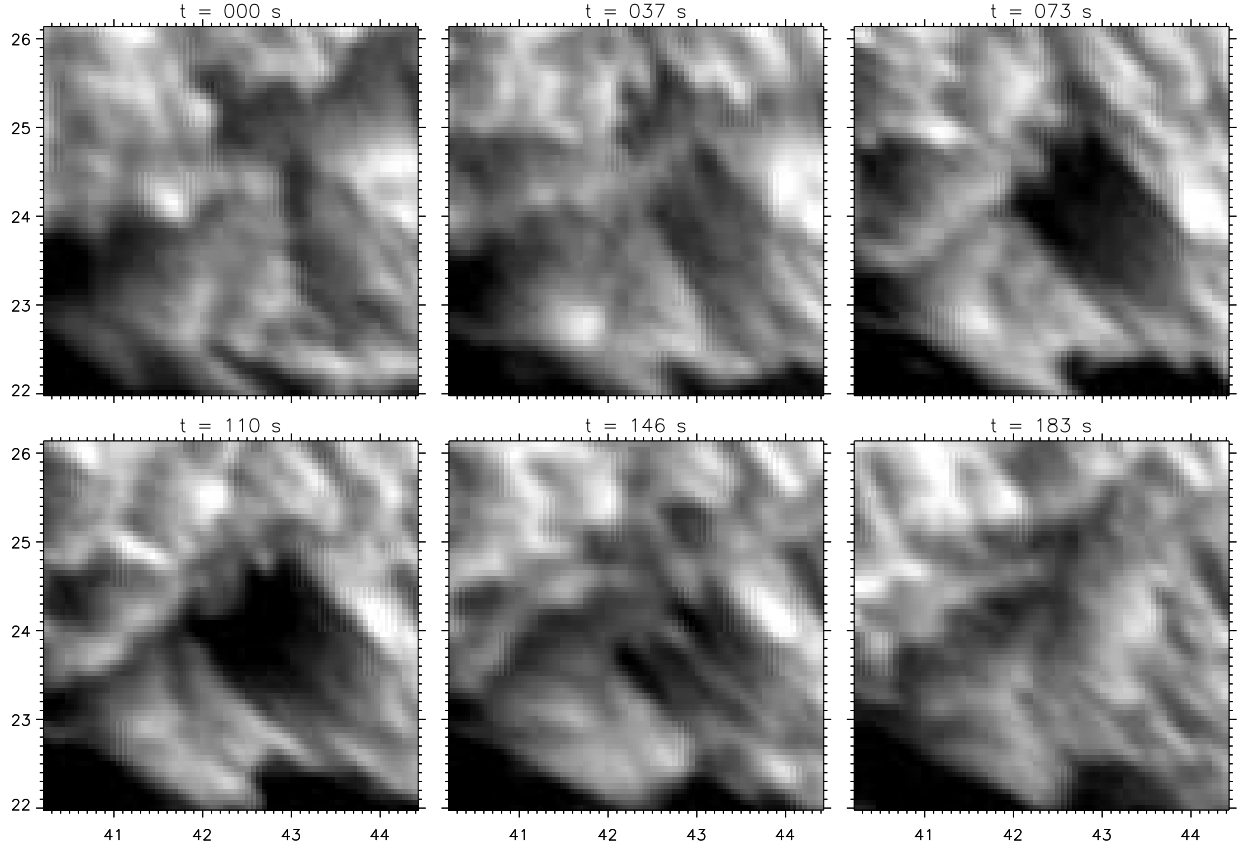


Fig. 5.— Snapshots in H $\alpha$  linecenter that show the temporal evolution of a dynamic fibril as it rises and retreats. This DF is relatively wide, short and lives for only three minutes. It is located in region 2. It shows clear evidence of substructure during its evolution, with different 'fingers' developing in a different fashion as a function of time. An mpeg-movie showing the temporal evolution of this DF is available online.

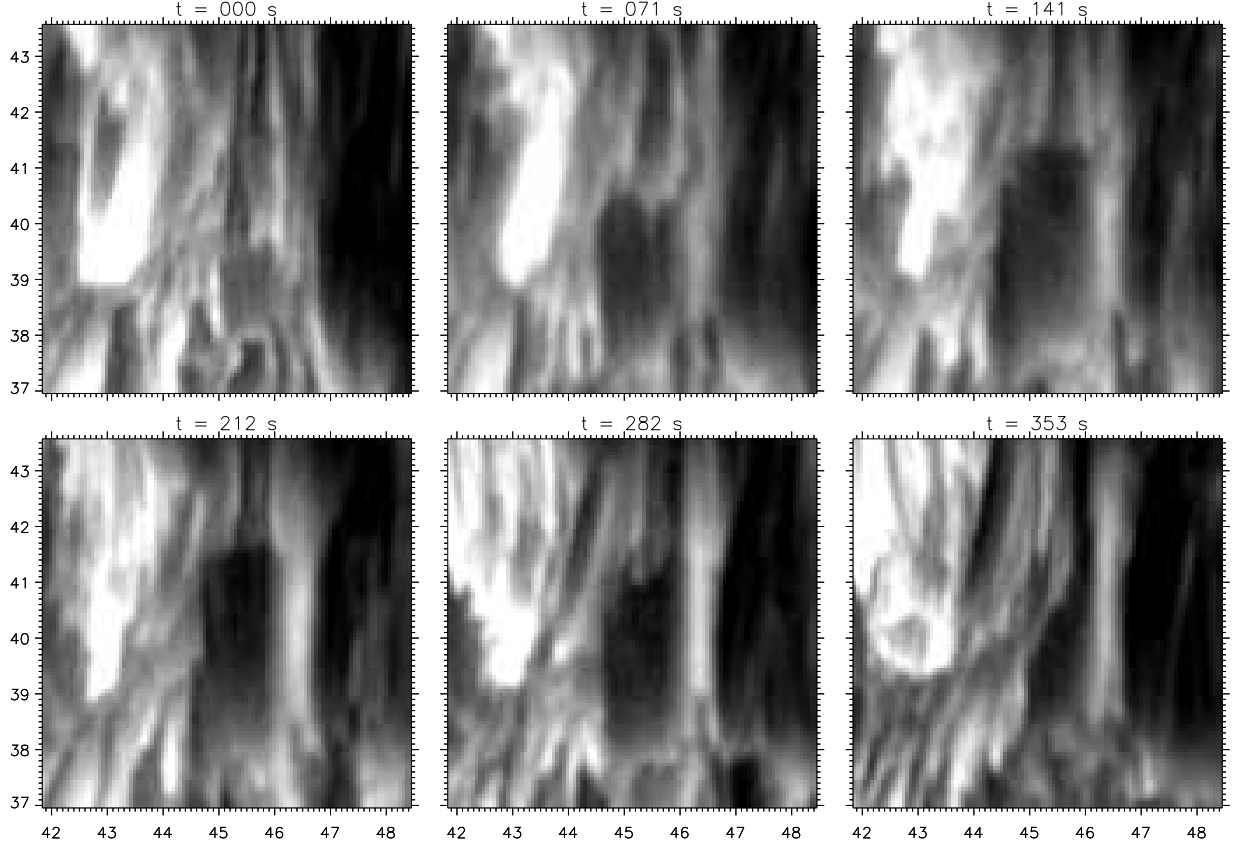


Fig. 6.— Snapshots in H $\alpha$  linecenter that show the temporal evolution of a dynamic fibril as it rises and retreats. This DF is very wide, long and relatively slow in its evolution. There are actually two DFs occurring along the same line-of-sight, with different temporal evolution, as evidenced in Fig. 7. An mpeg-movie showing the temporal evolution of this DF is available online.



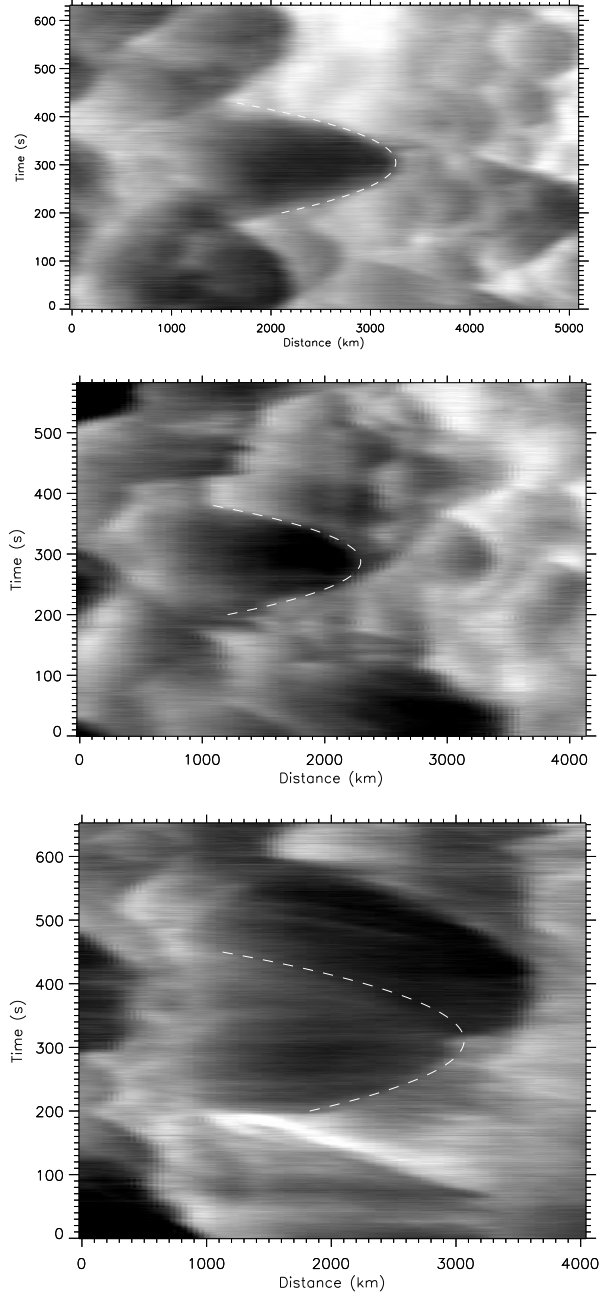


Fig. 7.— ‘xt’-plots for the three DFs illustrated in Figs. 4, 5 and 6. The dynamic fibril in the top panel (see Fig. 4) follows a near perfect parabolic path in its rise and descent. In the background other DFs are seen to follow similarly parabolic paths. The white dashed line indicates the best fit used to derive deceleration, maximum velocity, duration and maximum length. The dynamic fibril in the middle panel (Fig. 5) also follows a near perfect parabolic path. It does not maintain the same brightness throughout its life, with slow changes occurring along the axis of the DF during the ascent and descent. Some minimal effects from changes in the atmospheric seeing quality can be seen as brighter stripes in the horizontal direction. The dynamic fibril in the bottom panel (Fig. 6) is accompanied by a taller companion which seems to occur just behind it. The DF in the front (white dashed line) is somewhat brighter than the dark DF in the background.

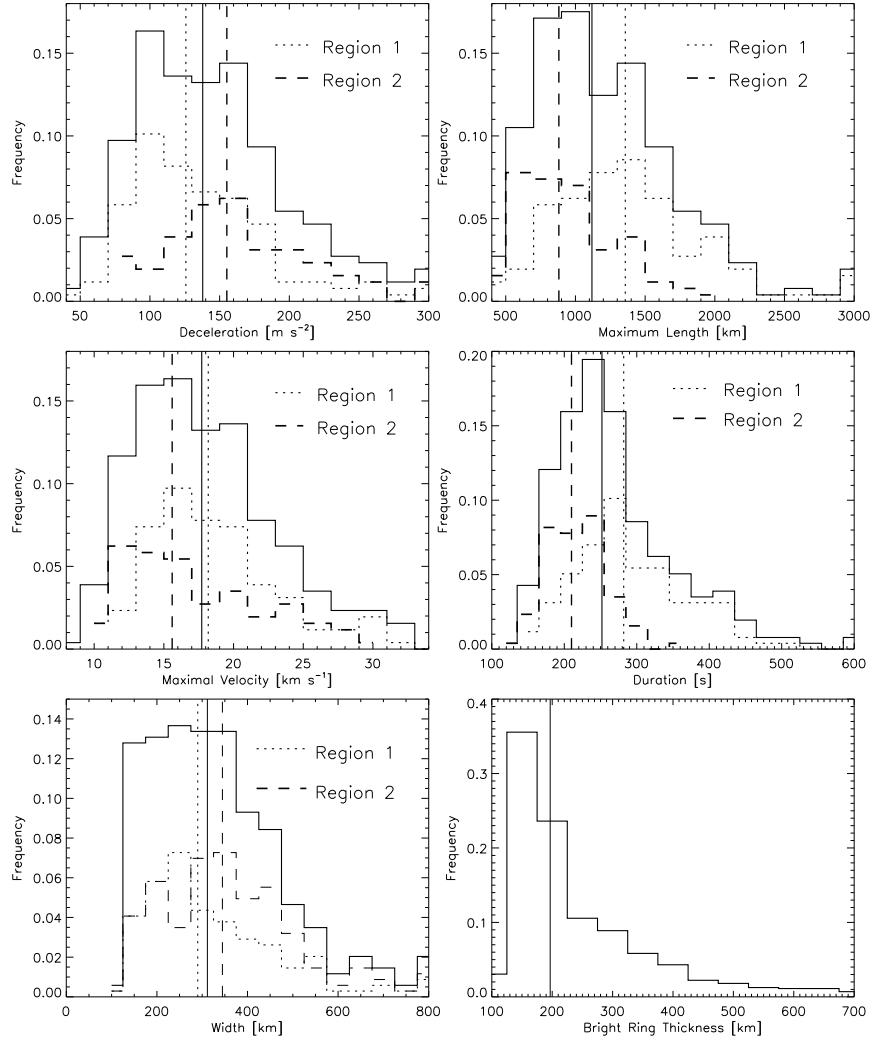


Fig. 8.— Normalized histograms for decelerations (upper left), maximum lengths (upper right), maximum velocity (middle left), duration (middle right), width (lower left) and thickness of the bright ring (lower right), measured for all 257 DFs (except widths which were measured for 91 DFs). The full vertical line in all plots indicates the median value of the distribution: a deceleration of  $136 \text{ m s}^{-2}$ , maximum length of 1100 km, maximum velocity of  $17.8 \text{ km s}^{-1}$ , duration of 250 s, width of 310 km and bright ring thickness of 190 km. The two regions illustrated in the right panel of Fig. 3 show clearly different distributions of the deceleration, maximum lengths and duration, as well as some differences in maximum velocity and width. Region 1 is indicated by dotted histograms and dotted vertical lines for the median values. This region shows lower decelerations ( $126 \text{ m s}^{-2}$ ), longer durations (280 s) and lengths (1350 km), slightly larger velocities ( $18.2 \text{ km s}^{-1}$ ) and slightly smaller widths (290 km) than region 2. Region 2 is indicated by dashed histograms and dashed vertical lines for the median values. It has higher decelerations ( $150 \text{ m s}^{-2}$ ), shorter durations (210 s) and lengths (880 km), slightly lower velocities ( $15.4 \text{ km s}^{-1}$ ) and slightly larger widths (340 km). The regional histograms are normalized to the total number of DFs.

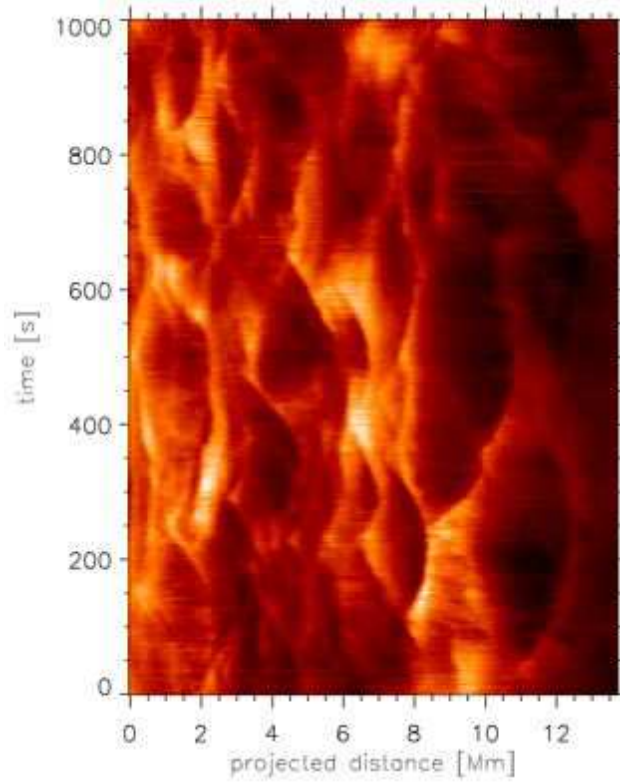


Fig. 9.— ‘xt’-plot for several DFs showing bright rings at their top end. This bright emission could be a measure of how steep the transition to hotter temperatures is at the top of the DF. Most DFs show some maximum of brightness at their top end. Measurements of the gradient at the top of DFs are given in the lower right panel of Fig. 8.

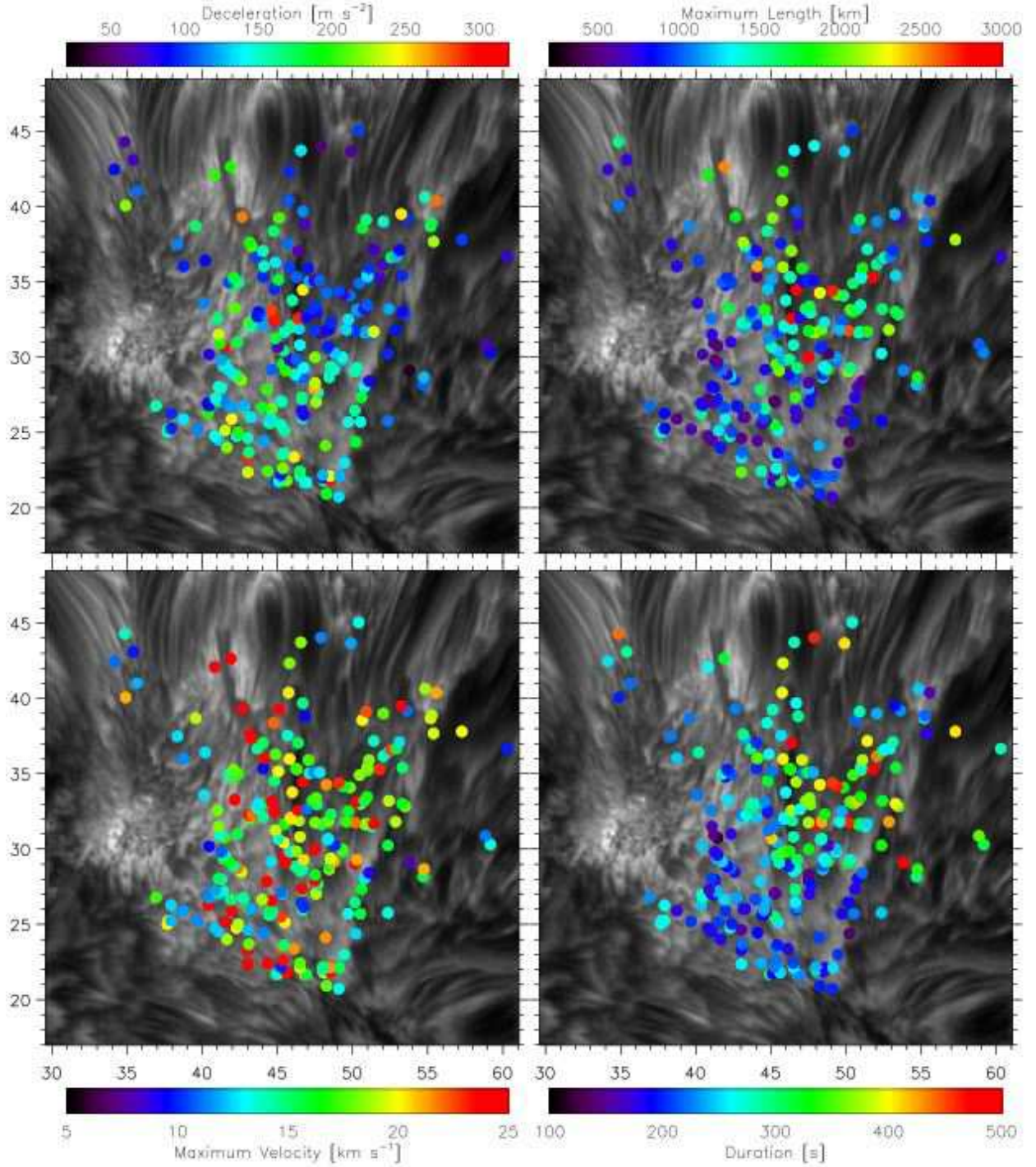


Fig. 10.— Differences in deceleration (upper left), maximum length (upper right), maximum velocity (lower left) and duration (lower right) for all measured DFs are illustrated as color-coded dots superposed on a H $\alpha$  linecenter image. DFs in region 1 (see right panel of Fig. 3) show lower deceleration, longer maximum length, slightly higher maximum velocity and longer duration than region 2.

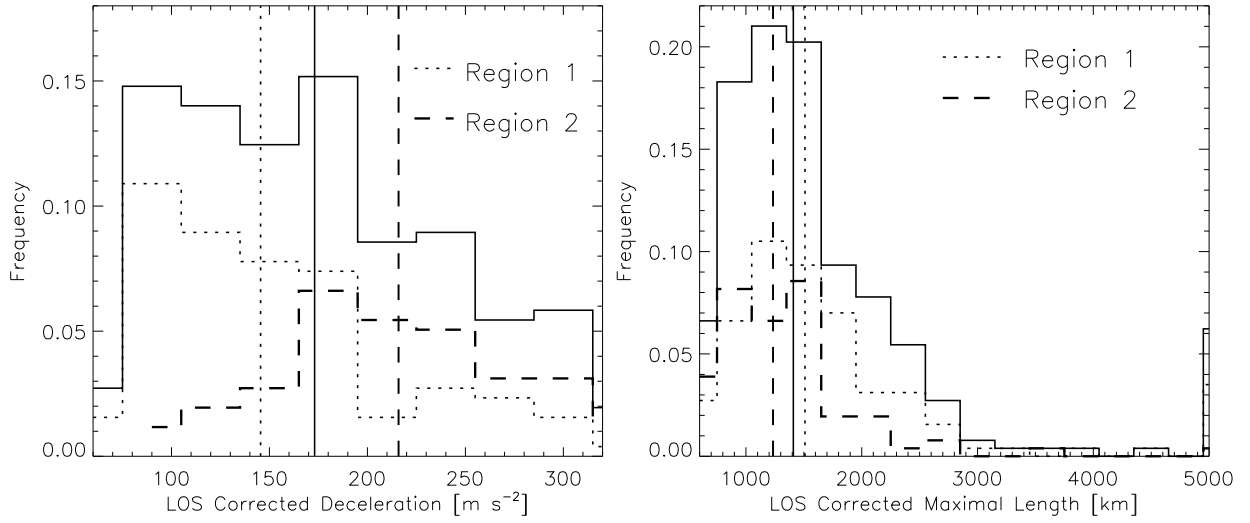


Fig. 11.— Normalized histograms for decelerations (left) and maximum lengths (right) that have been corrected for line-of-sight projection. We attempt to calculate the deceleration and maximum length that would be observed when the line-of-sight is perpendicular to the axis of the DF. We assume that the DF axis is aligned with the local magnetic field, as deduced from a potential field calculation, and take into account the actual line-of-sight vector of these observations. The regional differences do not qualitatively change: DFs in region 1 continue to be longer and have lower decelerations than those in region 2.

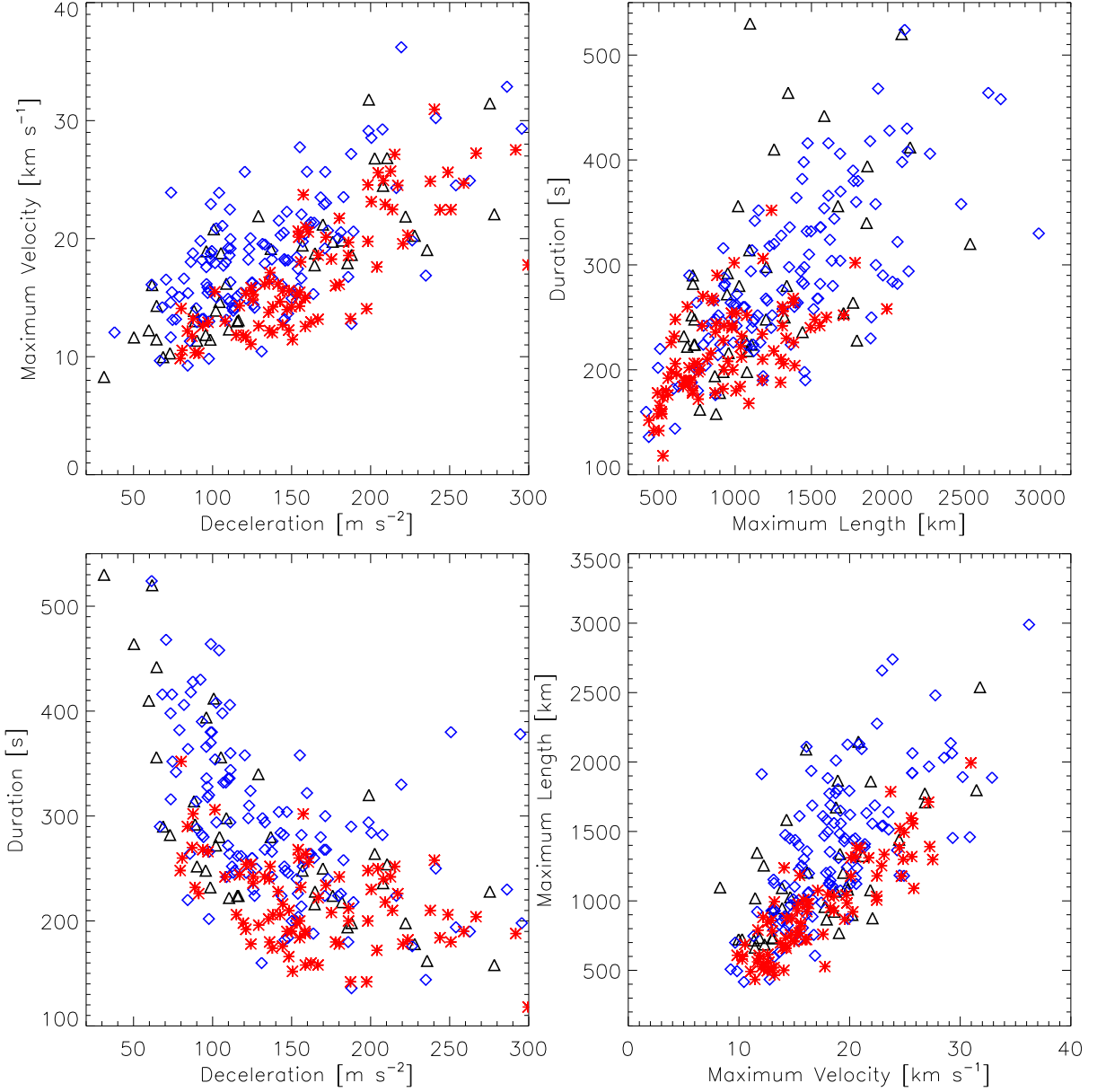


Fig. 12.— Scatterplots of deceleration versus maximum velocity (upper left), maximum length versus duration (upper right), deceleration versus duration (lower left), and maximum velocity versus maximum length (lower right). Clear linear correlations exist between deceleration and maximum velocity, maximum length and duration, and maximum velocity and maximum length. There is also a less well defined anti-correlation between deceleration and duration. DFs with higher maximum velocity typically suffer more deceleration (upper left), yet reach greater maximum lengths (lower right). DFs that are longer typically last longer. There are clear regional differences between region 1 (blue diamonds) and region 2 (red stars), which are also illustrated in Figs. 8 and 10. The scatterplots for the two regions often seem to have different slopes.

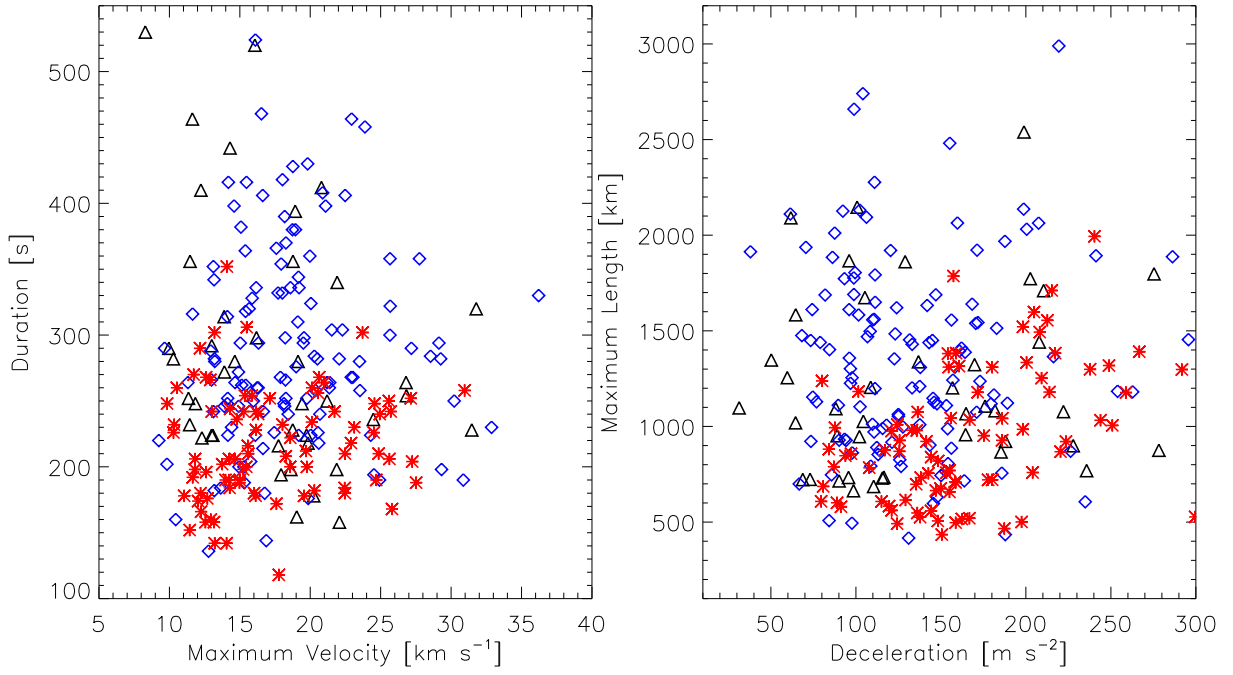


Fig. 13.— Scatterplots of maximum velocity versus duration, and deceleration versus maximum length. These plots do not show clear correlations. This may be caused by the wide spread in the scatterplots of Fig. 12, and the regional differences in many of the correlations.



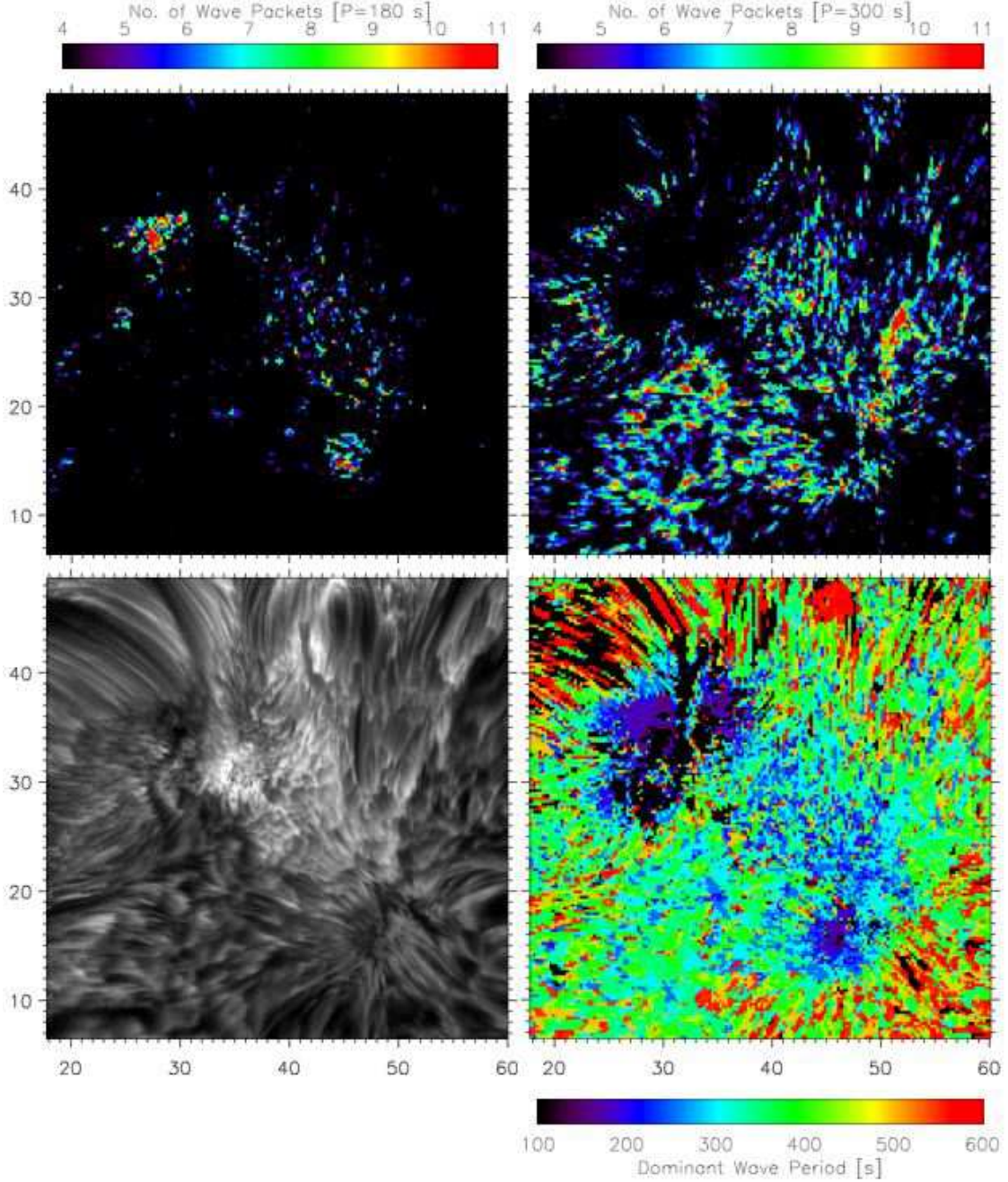


Fig. 14.— Results from a wavelet analysis of the 78 minute long  $H\alpha$  linecenter timeseries, a snapshot of which is shown in the lower left panel. The two top panels show, for each location of the lower left panel, the number of significant wave packets detected for waves with periods of 180 s (left) and 300 s (right). Locations with less than 4 wavepackets are not considered locations with significant power (shown as black). The lower right panel illustrates for each location which wave period dominates, i.e., contains the highest number of wavepackets with significant power. The two sunspots and region 2 are dominated by 3 minute power, region 1 by 5 minute power, and the highly inclined fibrils (e.g., in the superpenumbra) by oscillations with even longer periods.



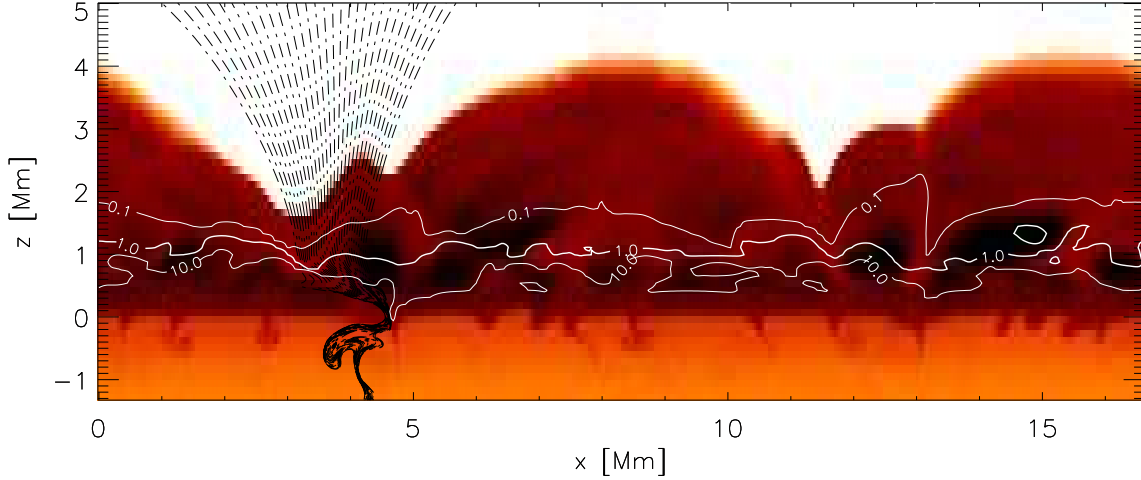


Fig. 15.— Snapshot taken from one of the 2D numerical experiments simulating the generation of a dynamic fibril. The logarithm of the temperature,  $T_g$ , is shown, set to saturate at  $\log T_g = 4.5$ ; the minimum temperature is roughly 2000 K ( $\log T_g = 3.3$ ). The vertical scale has its origin at the height where  $\tau_{500} = 1$ . Contours of plasma  $\beta$  are drawn in white where  $\beta = 0.1, 1, 10$ , with the  $\beta = 1$  contour thicker for clarity. In black are drawn magnetic field lines covering the region where dynamic fibrils ascend as a result of upwardly propagating shock waves. We find events that resemble observed dynamic fibrils in this region as well as in the corresponding opposite polarity region centered on  $x = 12$  Mm. Note the highly intermittent nature of the chromospheric temperature structure and the ubiquity of shocks outlined by regions of high  $T_g$ . These shock waves seem to preferentially enter the corona where the magnetic field lines also enter the corona. The position of the transition region does not change much in the regions between  $x = 5$  Mm and  $x = 12$  Mm, where the field is more horizontal. An mpeg-movie illustrating the dynamic evolution of the temperature and velocities is available online.

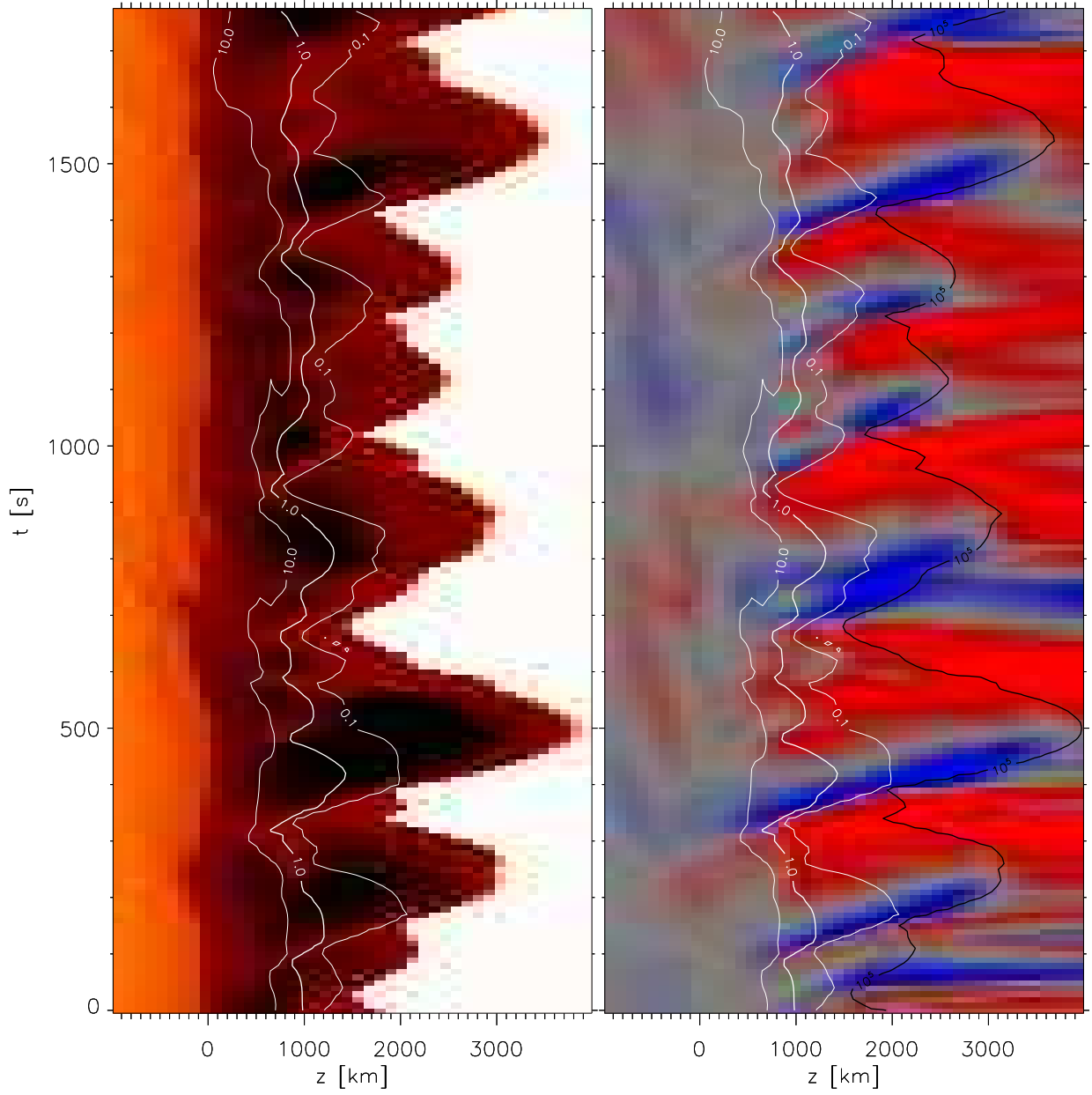


Fig. 16.— ‘xt’-plot of  $\log T_g$  (left panel) and the vertical velocity (right panel) as a function of height and time at horizontal position  $x = 4$  Mm in Fig. 15. The logarithm  $\log T_g$  of the temperature is set to saturate at  $\log T_g = 4.5$ ; the minimum temperature is roughly 2000 K ( $\log T_g = 3.3$ ). The velocity saturates at  $\pm 20$  km s $^{-1}$ , red color indicates downflows. Countours of plasma  $\beta$  are drawn in white where  $\beta = 0.1, 1, 10$ . A contour indicating the position of the transition region (where  $T_g = 10^5$  K) is shown in black in the right panel. Note how waves, generated as linear waves in the photosphere and forming shocks roughly 1000 km above  $\tau_{500} = 1$ , propagate upwards and push the upper chromosphere and transition region to great heights, several thousand kilometers above their equilibrium positions. The general appearance of this ‘xt’-plot is very similar to observed ‘xt’-plots (Fig. 7).

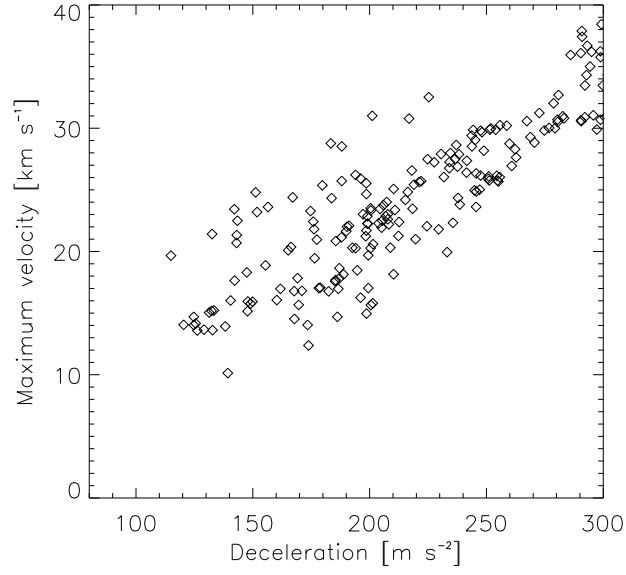


Fig. 17.— Scatterplot of deceleration versus maximum velocity from measuring several DF-like features in the numerical simulations. A comparison with the upper left panel of Fig. 12, reveals that the simulations reproduce the observed relationship, and range in deceleration and maximum velocity quite well.